POLYCRYSTALLINE CHROMIUM DOPED POTASSIUM NIOBATE SYNTHESIZED USING THE SOL-GEL METHOD

by

JASON PATICK GILCHIRST

(Under the Direction of Steven Lewis)

Abstract

Potassium Niobate (KNbO₃) doped with Iron is a well known photorefractive material in the optical region. There is, however, a need for photorefractive materials in the near infrared (NIR). Chromium doped KNbO₃ has been suggested as a possible candidate, and computer calculations and modeling show a photorefractive response above 0.4 eV in earlier studies. The latest studies have the photorefractive effect at 1 eV. Due to the volatility of K₂O it is problematic to fabricate $KNbO_3:Cr^{3+}$ as a congruent crystal. In this work, single phase (Cr³⁺) doped KNbO₃ was fabricated using the sol-gel method, which allows us to make a polycrystalline ceramic at low temperatures. Metal alkoxides, potassium ethoxide and niobium pentaethoxide were used as the precursor material. ${\rm KNbO_3:x\%~Cr^{3+}}$ were successfully prepared by reflux at 120 °C. The Cr³⁺ concentration in the host varied between 0.005 and 0.1 mol%. The obtained polycrystalline powder was characterized by using X-ray diffraction (XRD). No secondary phases were found in any of the doped or undoped samples, suggesting single phase orthorhombic KNbO₃. The X-ray diffraction data was used to study the effects of peak broadening by using the Williamson-Hall analysis technique. This was done in order to find the microstrain and crystallite size; to better understand changes in intensity of X-ray diffraction peaks as the concentration of trivalent chromium increased. Applying the madelung potential energy using the VESTA computer program and nearest neighbor potential energies the possible energy level that the Cr^{3+} ion lies within the host $KNbO_3$ was found. Further it appears that these theoretical calculations find agreement with prior theoretical models that established the ionization threshold of the chromium ions.

INDEX WORDS: KNbO₃ doped with Cr³⁺, Potassium Niobate, Chromium doped

Potassium Niobate, Williamson Hall Plot, VESTA, Madelung Potential

Energy, W-H Plot, Trivalent Chromium

POLYCRYSTALLINE CHROMIUM DOPED POTASSIUM NIOBATE SYNTHESIZED USING THE SOL-GEL METHOD

by

JASON PATICK GILCHIRST

B.S., North Carolina Agricultural and Technical University, 1998
M.S., North Carolina Agricultural and Technical University, 2001
M.S., The University of Georgia, 2015

A Dissertation Submitted to the Graduate Faculty of The University of Georgia in Partial Fulfillment of the

Requirements for the Degree

DOCTOR OF PHILOSOPHY

ATHENS, GEORGIA

 \bigcirc 2025

Jason Patick Gilchirst

All Rights Reserved

POLYCRYSTALLINE CHROMIUM DOPED POTASSIUM NIOBATE SYNTHESIZED USING THE SOL-GEL METHOD

by

JASON PATICK GILCHIRST

Major Professor: Steven Lewis

Committee: Kin Keung Mon

Heinz-Bernd Schüttler

Loris Magnani

Electronic Version Approved:

Ron Walcott Dean of the GraduateSchool University of Georgia May 2025

DEDICATION

This is dedicated to my wife, mother, father, and children, for always believing in me. It has been a long and hard journey with many ups and downs but they were with me through it all and helped me in any way that they could.

ACKNOWLEDGMENTS

I would first like to thank the Lord for getting me to this point. This has been a long arduous journey and I have spent much time praying and all of my prayers have always been answered. Thanks to Dr. Lewis for serving as my major professor and being such a great teacher overall. Thanks to Dr. Uwe Happek and Dr. Kin-Keung Mon, who stuck with me and kept working with me through this arduous journey. Dr. Happek has always come through for me when I needed him and kept working with me through the mistakes and setbacks. Dr. Mon has always been so encouraging throughout this process and helpful with advice along the way. Dr. Hoang Pham, one of Dr. Happek's graduate students came back to UGA on a weekly basis to help me fix up the lab and to fabricate the chromium doped potassium niobate using the sol-gel technique. Thanks to Dr. Schüttler for being on my committe and sticking with me over this long period of time to finish my thesis. Thanks to Dr. Loris Magnani for being on my committee. Dr. Magnani was my first graduate coordinator and one of the best coordinators, that helped me navigate through graduate school as I took my classes. Without him I do not know if I would have been able to make it through the first part of graduate school. Dr. Kanzo Nakayama was one of the best graduate coordinators at UGA, he always looked out for me and prodded me through the last steps of graduate school.

To my friends in my cohort in the physics department. Special thanks to Kellan Gibson for listening to me go over my presentations and helping me get my thesis dissertation working in latex format and Eric Suter, who was always available to help with understanding of the previous theoretical work that he worked on involving chromium doped potassium niobate. Also, another thanks to Eric Suter for use of his figures in my thesis research.

TABLE OF CONTENTS

		P	age
Ackn	OWLEDG	MENTS	V
List (of Tabl	ES	viii
List (of Figui	RES	ix
Снар	TER		
1	Introl	OUCTION	1
2	Backg	ROUND: THEORY AND EXPERIMENTAL METHODS	3
	2.1	PEROVSKITE STRUCTURE	3
	2.2	PRIOR THEORETICAL RESULTS	7
	2.3	PRIOR THEORETICAL RESULTS CONTINUED	9
	2.4	ELECTRONIC STRUCTURE	11
	2.5	CHROMIUM	12
	2.6	ELECTRON TRANSFER PROCESSES, BORN-HABER CYCLE	13
	2.7	PHOTOREFRACTIVE EFFECT	18
	2.8	WILLIAMSON-HALL METHOD	22
	2.9	CRYSTAL FIELD THEORY	26
	2.10	Tanabe Sugano	28
	2.11	Madelung Energy	29
	2.12	VESTA PROGRAM	32
	2.13	X-RAY DIFFRACTION	34
3	Sol Gi	EL Process	37

	3.1	INTRODUCTION	37
	3.2	Brief History	37
	3.3	Sol Gel Process Using the Reflux Method	39
4	ТЕСНІ	NIQUES FOR CHARACTERIZING Cr^{3+} and the Host Crystal	42
	4.1	Theoretical Results of the Photoexcitation Energy of	
		${ m Cr}^{3+}$ Within KNbO $_3$ Using the Nearest Neighbor Madelung	
		POTENTIAL	42
	4.2	Theoretical Results of the Activation Energy Cr^{3+} Within	
		$\mathrm{KNBO_3}$ Using VESTA Program to Calculate Madelung Po-	
		TENTIAL	48
5	SPECT	Tral Analysis of the host KNBO_3 and KNBO_3 :x% Cr^{3+}	56
	5.1	XRD Pattern of the host $\mathrm{KNBO_3}$ and $\mathrm{KNBO_3:}\mathrm{X\%}~\mathrm{CR}^{3+}$	56
	5.2	WILLIAMSON HALL ANALYSIS OF XRD PATTERN OF THE HOST	
		$KNBO_3$ and $KNBO_3:X\%$ CR^{3+}	59
6	Conc	LUSIONS	65
7	FuTul	RE WORK	67
Riblia)GRAPE	IV	69

LIST OF TABLES

2.1	Ion positions in cubic perovskite	3
4.1	Lattice cooridnates of ions used in Nearest Neighbor Site Potential for Madelung	
	Potential	45
4.2	Phase and Structural Parameters	45
4.3	Ionic Radii of Ions for Nearest Neighbor Site Potential	46
4.4	Lattice coordinates of the atoms in the $\mathrm{KNbO_3}$ base cell	50
4.5	Phase and Structural Parameters	51
4.6	Values Used to Calculate Energy Level Impurity Appears to be Located within	
	the Host KNbO ₃ Crystal	54
5.1	Values of crystallite sizes of $\mathrm{KNbO_3}$ and $\mathrm{KNbO_3:}\mathrm{x\%}$ $\mathrm{Cr^{3+}}$ where the concentration	
	tration of Cr^{3+} is increased from 0.005 to 0.1 mol%	63

LIST OF FIGURES

2.1	Cubic perovskite unit cell. Blue spheres represent the A cations, yellow	
	spheres represent the B cations, and the red spheres represent oxygen anions,	
	which form an octahedra around the B cations	4
2.2	(a) Atomic displacements from cubic perovskite aristotype positions for phases	
	changes of KNbO ₃ where the center of mass is not displaced. (a) Tetragonal	
	phase, (b) orthorhombic phase, and (c) rhombohedral phase. In all the phase	
	transitions the oxygen octahedra remains rigid and is displaced as unit along	
	the (a) [001], (b) [011], (c) [111]. The last sketch (d) shows how the rigid	
	oxygen octahedra oscillates in one of the unstable zone-boundary modes	6
2.3	2x2x2 supercell of the orthorhombic cell that was used in prior theoretical	
	work. The two selected atoms indicate where the dopant species goes and the	
	oxygen atom is removed. Cyan spheres are K, green spheres are Nb, and red	
	spheres are O atoms [11]	8
2.4	The picture of the structure shows a defect within a single orthorhombic cell	
	of KNbO ₃ . The cyan spheres are the K atoms, the green spheres are the Nb	
	atoms, the red spheres are the O atoms, and the single orange sphere is the Cr	
	dopant. The O atom with the cross-hair and yellow outline is the site vacancy	
	[12]	10
2.5	Energy bands and projected density of states of the valence and conduction	
	bands of pure orthorhombic KNbO ₃ [3]	11
2.6	Localized and electron transfer processes	15

2.7	Photorefractive process that starts with the intensity distribution of the in-		
	terference pattern, charge photogeneration, charge transport and distribution		
	after migration and trapping, space-charge field. Finally the index modulation		
	is shown. [37]	20	
2.8	A varying index or refraction, electric field, charge distribution, and intensity		
	shifted due to the photorefractive effect.	21	
2.9	A Williamson-Hall plot showing the linear relationship and the slope as an		
	example. The figure shows several reflections as data points. Where the strain		
	component is the slope and the size component comes from the intercept	24	
2.10	Schematic view of the Size of crystallite in reference to that of Particle Size .	25	
2.11	The splitting of the d-orbitals of a transition metal due to the d_{z^2} and $d_{x^2-y^2}$		
	orbitals increase in energy while the, d_{xy} , d_{xz} , and d_{yz} orbitals decrease in		
	energy. The geometry of the two \mathbf{e}_g states and three \mathbf{t}_{2g} states are shown on		
	the right. [3]	27	
2.12	Tanabe-Sugano energy level diagram for $3d^3$ system. Diagram obtained from		
	Henderson and Imbusch [6]	29	
2.13	NaCl Image obtained from Gelest [37]	31	
2.14	Essential components of an X-ray Diffractometer. Diagram obtained from G.		
	Harrington and J. Santiso [51]	35	
3.1	Sol gel process involves precursor materials that are processed through several		
	sol gel synthesis routes. Image obtained from Gelest [37].	38	
3.2	The Skelatal Formula of the reflux reaction of potassium ethoxide and niobium		
	pentaethoxide	40	
3.3	The reflux chamber used in this project. The condenser is the clear tube on		
	top with the two hoses connected for a constant flow of water	41	
4.1	Nearest Neighbor potential energy level diagram showing the photoexcitation		
	energy level of Cr ³⁺ impurity site	43	

4.2	Unit cell 3-D picture from VESTA, used in calculations of the Madelung		
	Energy	53	
4.3	Side-by-Side view of KNbO $_3$ supercells	54	
5.1	XRD of undoped KNbO $_3$ using Co K $lpha$ fabricated in the Happek Lab	56	
5.2	XRD of KNbO3: 0.005, 0.01, 0.05, and 0.1 mol% Cr^{3+} using $Co~K\alpha$ fabricated		
	in the Happek Group Lab.	57	
5.3	3-D view of XRD of x% $\rm Cr^{3+}~KNbO_3$ using Co $\rm K\alpha$ fabricated in the Happek		
	Lab	58	
5.4	Williams-Hall Plot KNbO_3	60	
5.5	Williamson-Hall Plot KNbO3: 0.005 mol% Cr^{3+}	60	
5.6	Williams-Hall Plot KNbO3: 0.01 mol% $\rm Cr^{3+}$	60	
5.7	Williamson-Hall Plot KNbO3: 0.05 mol% Cr^{3+}	60	
5.8	Williamson-Hall Plot KNbO ₃ : 0.1 mol% Cr ³⁺	61	

Chapter 1

Introduction

Potassium niobate $(KNbO_3)$ is an ionic solid that crystallizes in the perovskite type structure and was discovered in 1949 [1]. KNbO₃, exhibits the ABO₃ stoichiometry and belongs to a well known class of ferroelectrics, which has been investigated intensely due to its large electro-optic coefficients, nonlinear optical coefficients, holography, optical memory storage, and electromechanical coupling factors for various electro-optical and nonlinear optical devices. An added benefit is that it is less toxic than other ferroelectric materials possesses higher chemical stability and environmentally friendly. Below the Curie temperature of T_C =435 °C, single crystal KNbO₃ is ferroelectric and undergoes a series of phase changes. These phase changes include the cubic to tetragonal phase at 435 °C, tetragonal phase to the orthorhombic phase at 225 °C, and orthorhombic phase to rhombohedral phase at - 50 °C [2]. Another property which will be further explored in the current project is that of the photorefractive response of KNbO₃ and the study of different dopants in KNbO₃ which is an active research field. KNbO₃ doped with Iron (Fe) is known to have a photorefractive response in visible spectral region. There is a need for a photorefractive response in the near infrared (NIR). $KNbO_3$ doped with trivalent chromium (Cr^{3+}) has been suggested as a material that will have a photorefractive response in the NIR [3].

Laser heated pedestal growth [LHPG] method to crystalize single-phase KNbO₃ was found to be problematic, possibly due to the volatility of K_2O [4] [5]. Another technique that has been used to counter this problem is to fabricate the Cr^{3+} doped KNbO₃ powder by sol-gel process. This allowed fabrication of the polycrystalline ceramic at lower tempera-

tures, thus preventing the issue of the volatility of K₂O at low temperatures. Lattice defects such as impurities generally introduce some levels in the forbidden gap between the extended states of the lattice. The environment of the host influences the impurity electrons due to the crystal field of certain symmetry and strength, therefore causing energy splitting and shifting of the free ion orbitals [6]. It has been shown that an understanding of the host-impurity system requires the incorporation of excitation processes that involve the impurity electronic states and the extended electronic states of the host lattice, in other words the valence and conduction band. This leads to the donor and acceptor-like model for the impurity host system. This system has been a very useful model in doped semiconductors [7]. In this dissertation the possible energy level at which we find Cr³⁺, using theoretical models that incorporate the madelung potential energy. In one such model the nearest neighbor potential energy was used in conjunction with the ionization energy of Cr³⁺ in a vacuum. The other theoretical model uses the Madelung Potential energy found using the VESTA program [8] along with the electron transfer energy process. Also the Williamson-Hall plot will be used to further examine the nature of the X-ray Diffraction (XRD) results found, which appear to show changes in intensity along with increasing dopant in the potassium niobate host crystalline material. In the next chapter the perovskite structure will be discussed along with prior theoretical results and the theory behind the experimental and theoretical techniques used to characterize polycrystalline chromium doped potassium niobate. In chapter 3 the experimental method for preparing the polycrystalline doped samples will be discussed. In chapters 4 and 5, techniques for theoretically measuring where the energy level at which ${\rm Cr}^{3+}$ dopant lies below the conduction band of ${\rm KNbO}_3$ along with XRD analysis of the polycrystalline samples. The conclusion is given in chapter 6 and the thesis concludes with a discussion of our future research direction in chapter 7.

CHAPTER 2

BACKGROUND: THEORY AND EXPERIMENTAL METHODS

2.1 Perovskite Structure

Perovskite is the name given to any mineral with the same crystal structure as the mineral CaTiO₃. The mineral samples of CaTiO₃ were discovered by Gustav Rose in the Ural Mountains, in 1839 and named after the Russian mineralogist, Count Lev Aleksevich von Perovski. Structurally, ABO₃ type perovskite is paraelectric above the curie temperature, due to the high symmetry of the cubic phase unit cell. In this phase the A cation is located at the corners of the cube, the B cation is body centered, and the O anions are face centers which can be seen in Fig 2.1

The B cation is surrounded by an octahedron cage where the 6 Oxygen anions are symmetrically arranged defining the vertices of said octahedron. The traditional view of the perovskite lattice consists of small B cations within an oxygen octahedron, and larger, 12-fold coordinated cations [9]. The ideal cubic perovskite environment dictates that with any two cations, the one with the smaller size will occupy the B site while the larger one is favored for the A site. The sum of their charges is +6, which in turn balances exactly with

Table 2.1: Ion positions in cubic perovskite.

Site	Location	Co-ordinates
A cation	(2a)	(0,0,0)
B cation	(2a)	(1/2, 1/2, 1/2)
O anion	(6b)	(1/2, 1/2, 0)(1/2, 0, 1/2)(0, 1/2, 1/2)

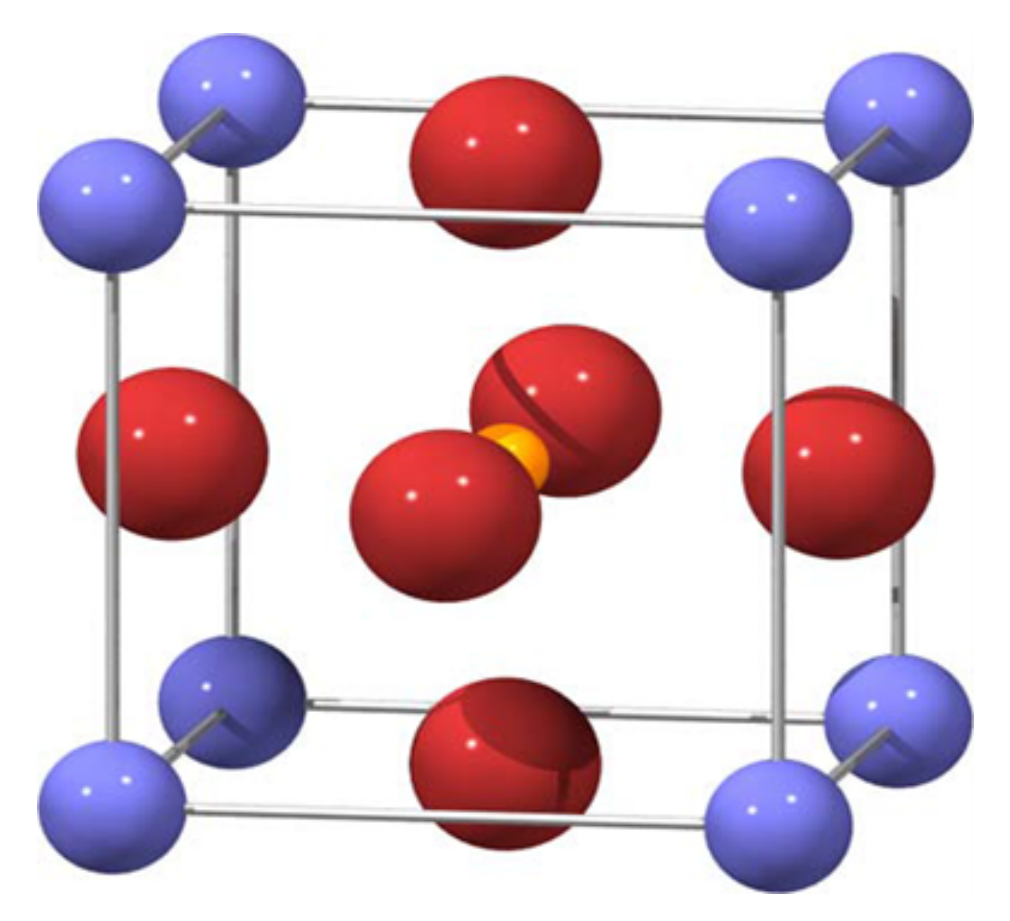


Figure 2.1: Cubic perovskite unit cell. Blue spheres represent the A cations, yellow spheres represent the B cations, and the red spheres represent oxygen anions, which form an octahedra around the B cations.

the 3 O²⁻ anions, rendering the unit cell electrically neutral. In most perovskite structures the A cation is an alkaline metal, such as but not limited to, Li, Na or K with oxidation state +1 or an alkaline earth metal, such as, Mg, Ca, Ba with oxidation state of +2 or a rare earth element La with an oxidation state of +3. The B cation site is occupied by transition metals with oxidation states +5, +4 or +3, respectively. There are several perovskites that exhibit one or more ferroeletric or antiferroeletric structural phase transitions. Examples of these are BaTiO₃, PbTiO₃, NaNbO₃, and KNbO₃. Structural changes in perovskite structures are important factors in the change of the dipole moment which leads to ferroelectric effects. Finally, two of the most important and most used lead-free ferroelectric

materials are KNbO₃ and LiTaO₃. These materials are of the $A^{1+}B^{5+}O_3$ type perovskite family. The structural changes of KNbO₃ have been studied by A.W. Hewat [2] using neutron scattering. When a perovskite, such as KNbO₃, is in the cubic phase it is electrically neutral but as the temperature lowers, spontaneous polarization occurs. This occurs when the high symmetry of the cubic phase is broken at T_C . These structural changes at lower temperatures have been studied by A.W. Hewat using neutron diffraction measurements of powdered crystals. During changes in phase the oxygen octahedra has been shown to be rigid due to the strength of the oxygen-oxygen bond in comparison to the bonds between potassium-oxygen and niobium oxygen. These structural transitions can also be attributed to the condensation of soft lattice vibrational modes. The magnitudes and directions of these atomic displacements account for the observed changes in the spontaneous polarization of KNbO₃ when the effective atomic charges are estimated from infrared and dielectric data. Figure 2.2 shows the atomic displacements from the cubic perovskite aristotype positions for various phase changes of KNbO₃ from cubic to rhombohedral phase, where the center of mass is considered undisplaced [2].

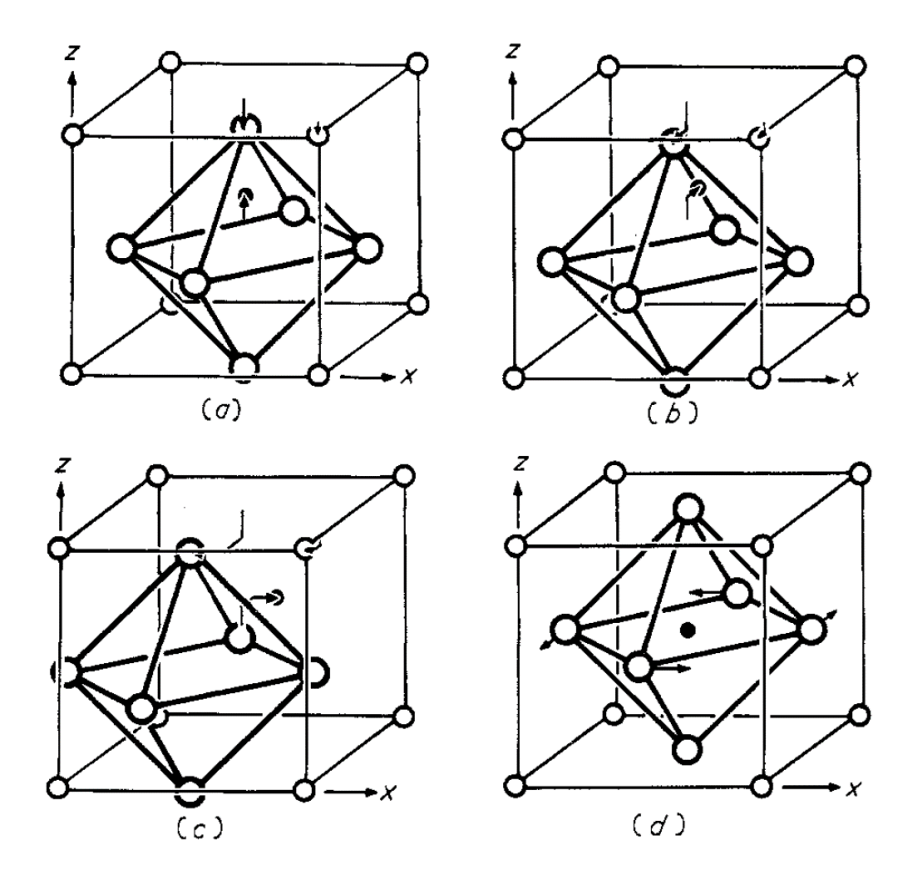


Figure 2.2: (a) Atomic displacements from cubic perovskite aristotype positions for phases changes of KNbO₃ where the center of mass is not displaced. (a) Tetragonal phase, (b) orthorhombic phase, and (c) rhombohedral phase. In all the phase transitions the oxygen octahedra remains rigid and is displaced as unit along the (a) [001], (b) [011], (c) [111]. The last sketch (d) shows how the rigid oxygen octahedra oscillates in one of the unstable zone-boundary modes.

Figure 2.2 (a) shows the transition of cubic-tetragonal at a temperature of 435 °C, which is also the Curie temperature for KNbO₃. The KNbO₃ aristotype cubic perovskite structure has a unit cell of around 4 Å. At the transition, the space group changes from Pm3m to P4mm, where the atoms are displaced by around 0.1 Å, which produces an electric dipole along the [001] of each cube unit cell. Figure 2.2 (b) shows the transition of tetragonal-orthorhombic. During this transition the two soft modes degenerate with the mode responsible for the cubic-tetragonal transition are stabilized by this transition at 225 °C, where one of the modes condenses to the orthorhombic phase, which has a net polarization along [011].

The space group then changes from P4mm to Amm2 during this phase transition. As in the cubic-tetragonal transition the oxygen octahedra remains comparatively undistorted. Figure 2.2 (c) shows the orthorhombic-rhombohedral transition at -10 °C. The rhombohedral unit cell can be described as a slight stretching of the aristotype cubic cell along [111], changing the space group from Amm2 to R3m [2]. Figure 2.2 (d) shows the rigid octahedra oscillating in one of the low-frequency zone-boundary modes responsible for the observed antisotropy in the mean-square displacement of the oxygen atoms.

2.2 Prior Theoretical Results

This experimental research was done in order to test prior theoretical models. Potassium niobate (KNbO₃) is a member of a family of ferroelectric photorefractives, with large electrooptic coefficients and stays in an orthorhombic crystal system over a wide range of temperatures (-50°C - 220°C). Unavoidable defects which are present in experimentally fabricated $\mathrm{KNbO_3}$ have charge centers that are smaller than the 3.3 eV band gap, which provide the charge centers for photoexcitation [10]. These levels can be influenced by doping of the crystal melt. The dopants will affect the different photorefractive performance parameters, such as but not limited to carrier mobility, trapping time, electro-optic coefficient, etc. In prior theoretical research it has been found that KNbO₃ has a spectral response into the near infrared, which can be achieved through doping. This is what lead to the theoretical proposition that the photorefractive performance parameters of KNbO₃ due to dopants that would generate properties tailored to infrared (IR) applications. A theoretical model based on first-principles was a useful tool in gaining a detailed understanding of the mechanisms involving the formation and stabilization of different impurities and associated vacancies. Models and electronic-related results were made using Density Functional Theory (DFT), when pure KNbO₃ was doped with 3d transition metal impurities, with Cr showing the closest possibility of photorefractivity in the NIR. A 2 x 2 x 2 super cell with 80 atoms was chosen to maintain computational efficiency and doping concentration. This model was used to investigate defects and impurities within the theoretical model. This corresponds to a doping concentration of 6.25%, which is well above the experimentally realized dopant concentration of $\approx 0.1\%$.

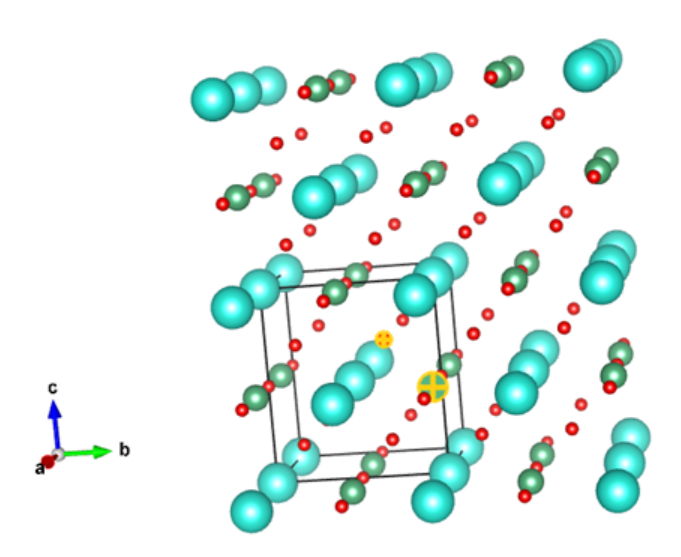


Figure 2.3: 2x2x2 supercell of the orthorhombic cell that was used in prior theoretical work. The two selected atoms indicate where the dopant species goes and the oxygen atom is removed. Cyan spheres are K, green spheres are Nb, and red spheres are O atoms [11]

Figure 2.3 shows the 2x2x2 supercell, where the two atoms with the yellow, bullseye indicates the two selected atoms where the dopant goes and the oxygen that gets removed to make the defect complex respectively. The color key for the pictures are cyan shperes for Potassium (K), Green spheres are Niobium (Nb), and red spheres are Oxygen (O). The theoretical calculations indicate that an energetically favorable way to maintain charge neutrality is if one of the Nb⁵⁺ ions is replaced by a 3d transition metal preferably Cr^{3+} ion and to remove one O^{2-} ion near the impurity. This results in an impurity-vacancy complex. Also the ionic radius of Cr^{3+} is 0.62 Å, which is comparable to the ionic radius of Nb⁵⁺ which is 0.64 Å.

2.3 Prior Theoretical Results Continued

Since the prior theoretical work by Mahou et al. there has been further theoretical modeling using the same 2 x 2 x 2 supercell was done by Suter et. al.[3][12]. In these calculations the doped systems were created using a 2 x 2 x 2 supercell containing 80 atoms. The defect models were used to find a more exact origin of the IR sensitivity introduced by 3d transition metals. The knowledge that transition metals preferentially occupy the Nb sites within crystals[13]. It is generally thought that at this site the substitution of the dopants assume a +3 charge state partially on the basis that their atomic radii in this charge state are closer to the Nb⁵⁺, which should minimize stress on the cell and lead to more favorable energy formations. With this assumption, the removal of an oxygen atom in the cell would free two electrons which would lead to some sort of charge compensation which would bind the dopant to attain the +5 charge [14].

The models examined a substitution of the Nb site with Ti, V, Cr, Mn, Fe, Co, and Ni, which are 3d transition metals. The band structures and projected densities of states were examined when induced with a charge-compensating oxygen vacancy in either the first coordination shell of O atoms around the dopant or in a shell that is as far away from the dopant as possible within the supercell which is shown within the Figure 2.3. When the oxygen vacancy is near the dopant the model is called the coordinated vacancy model and when the oxygen vacancy is as far away as possible within the supercell it is called the uncoordinated vacancy model. KNbO₃ has a high static dielectric constant which significantly reduces the electrostatic interaction between periodic replicas, which is good in the case of the uncoordinated vacancy model where the oxygen vacancy is approximately 7.5 Å away from the dopant. The models aim to represent the effects of the dopants when the charge-compensating vacancy either does or does not disturb the crystal field locally surrounding the dopant [15].

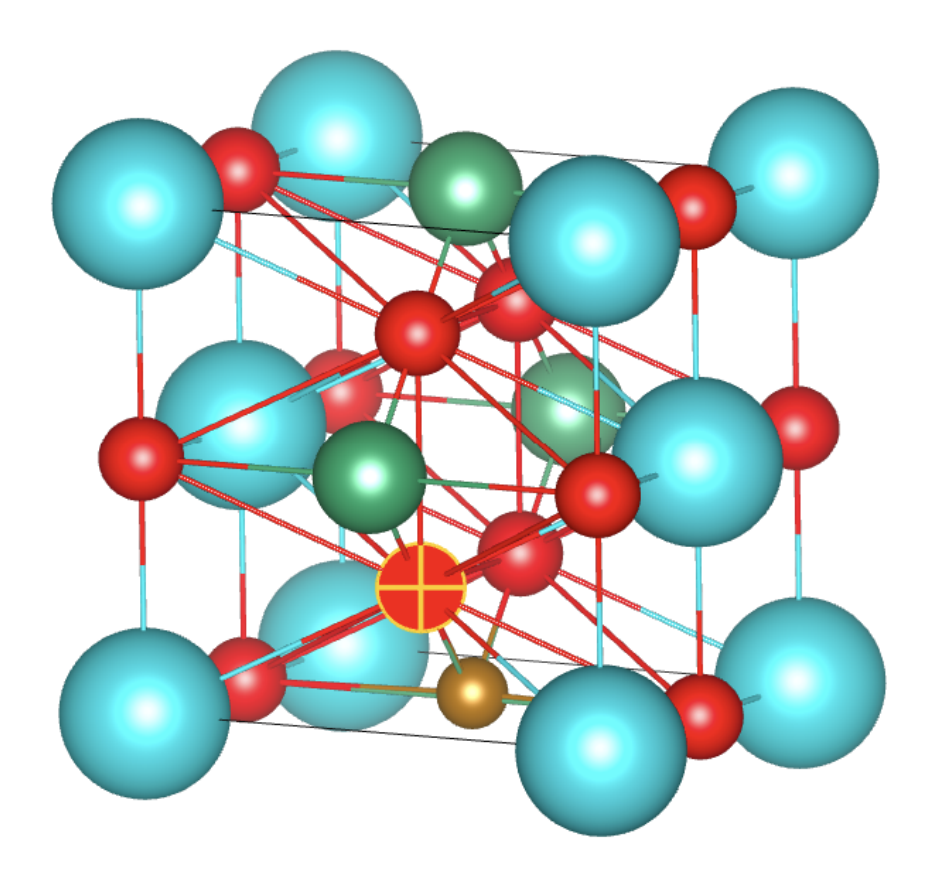


Figure 2.4: The picture of the structure shows a defect within a single orthorhombic cell of KNbO₃. The cyan spheres are the K atoms, the green spheres are the Nb atoms, the red spheres are the O atoms, and the single orange sphere is the Cr dopant. The O atom with the cross-hair and yellow outline is the site vacancy [12].

Comparisons of the coordinated and uncoordinated vacancy models reveals that the coordination of the O vacancy with the Cr impurity shifts just barely down in the energy out of the conductions band. As with prior theoretical results Cr doping has been demonstrated to significantly affect the optical properties of other oxide systems and is expected to represent a strong candidate for KNbO₃ [16][17][18]. The main interest in KNbO₃:Cr are a cluster of three nearly degenerate t_{2g} states located about mid-gap that occur only in the spin-up band structures.

2.4 Electronic Structure

An approach for calculating the impurity-host electronic structure originates from the oneelectron picture and could be classified in terms of band versus bonds [19]. The bandstructure approach is generally preferred for studying the bulk properties of materials because of the extended nature of the electronic states in periodic systems. The effect of impurities can be calculated within supercells. The picture that can be found using supercell calculations includes the impurity as a periodically occurring lattice point. This result displays the states corresponding to the impurity but within the states of the host electrons.

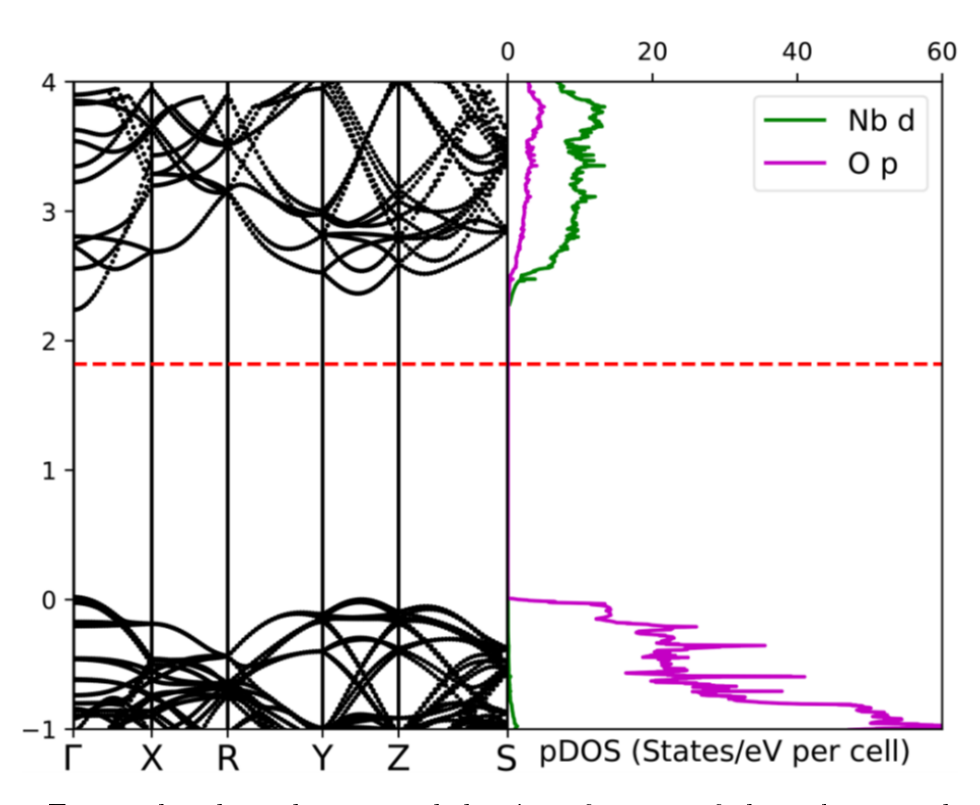


Figure 2.5: Energy bands and projected density of states of the valence and conduction bands of pure orthorhombic KNbO₃ [3].

To find the electronic band structure and projected density of states of pure orthorhombic $KNbO_3$, calculations for the band structure of different host materials have been successfully performed and correlating the electronic energy dispersion curves in the 1^{st} Brillouin zone have been obtained [20–22].

The band structure and projected density of states of pure orthorhombic KNbO₃ are shown in the Figure 2.5, which is an important factor in determining the population energetics of the dopant 3d states involves considerations of the local crystal field experienced by the dopant ion. The geometry of the surrounding chemical environment institutes an electrostatic perturbation that modifies the position of the dopant sites, in particular. The dopant ion being surrounded by an ideal octahedron will, therefore, experience a crystal-field splitting of the d orbitals and the degenerate 3d states will split into a degenerate pair of e_g states and a degenerate triplet of t_{2g} states. This shows that the valence band of KNbO₃ largely comes from Oxygen 2p states while the conduction band comes from the Nb 4d states, with some evidence of hybridization between the two sets of orbitals.

2.5 Chromium

Chromium is a transition metal that is hard and silvery. It is a chemical element with the periodic symbol of Cr. The chemical element chromium has an atomic number of 24. Chromium was discovered by French Chemist Louis-Nicolas Vauquelin in 1797 [23]. This red lead was a compound with selenium and iron components, the miner was actually crocoite that has a chemical formula of PbCrO₄. While working with a mineral called Siberian red lead, now called crocoite, Vauguelin dissolved the mineral in hydrocholoric acid and removed the lead. What was then produced was chromium trioxide, CrO₃. Vaugeulin also heated the CrO₃ in a charcaol oven which isolated the metallic chromium. Chromium is reflective and has a metallic luster when polished. It is used in decoration and applied to

electroplating. Neutral chromium has 24 electrons and that electron configuration consist of 1s²2s²2p⁶3s²3p⁶3d⁵4s¹. Chromium is an element that has a configuration that violates the Aufbau principle. The Aufbau principle is a general rule that guides the filling of electronic orbitals in atoms as they build from lowest energy level to the highest. In the case of chromium the expected configuration is deviated from due to stability of the halffilled 3d subshell in chromium [24]. The 3d⁵ configuration is more stable than the expected 3d⁴ and 4s² configuration due to the increased electron pairing energy required to fill the 4s orbitals. This deviation occurs in other transitions metals and is therefore not unique to chromium. Trivalent chromium is a naturally found ion, which can be found in some foods. In the +3 valence state, the chemistry of chromium is dominated by the formation of stable complexes with both organic and inorganic ligands [25]. Trivalent chromium like rare earth/transition metal ions (i.e. $\mathrm{Re^{3+}/Tr^{3+}}$) doped in glasses, ceramics and phosphors are used in many applications in different fields and in everyday life [26]. They are used in laser devices, display devices, bright light emitting diodes (LEDs), color tunable light sources, etc. An interesting note about these materials is that they can convert infrared light to visible/UV light and vice-versa [27]. The conversion of UV light to the near infrared is useful for enhancing efficiency of solar cells. Trivalent chromium ion with the configuration of 3d³ has been used as sensitizer as well as activators in different hosts matrices. The ²E state of Cr³⁺ ion is a long-lived state, which gives long lasting phosphorescence.

2.6 ELECTRON TRANSFER PROCESSES, BORN-HABER CYCLE

Throughout the present work the impurity states introduced in the electronic structure of a host insulator will be important to this research project. It is a problem that can be formulated under the condition that the perfect lattice potential and the impurity potential can be condensed to the one-electron potentials V_i and U_i , respectively, and the proper sets of basis functions can be found to describe different electronic states. This formalism has been applied with great success in understanding the bound states of impurities within

semiconductors and insulators [28]. The solution of the stationary Schrodinger equation for N-electron occupied states

$$\Sigma_i^N(\frac{p_i^2}{2m} + V_i^{per} + U_i)|\phi_1\phi_2...\phi_i..\phi_N\rangle = E|\phi_1\phi_2...\phi_i..\phi_N\rangle, \tag{2.1}$$

determines both the lattice and impurity electronic states and it is the difference of the two potentials, V and U, that play an important role in shaping the character and position in energy. The situation where there are localized impurity levels present in the bandgap in addition to the delocalized states belonging to the valence and conduction bands (VB, CB) of the host is shown schematically in Figure 2.6. Figure 2.6 shows an idealized absorption spectra illustrating absorption transitions. This process shows that in the presence of an incident radiation of energy $h\nu$ the simplified electronic processes that takes place depends on the electronic configuration (P³⁺/P⁴⁺) of the impurity.

Resonant absorption at a photon energy of $h\nu_a$ that leads to a transition between two localized, well determined energy levels: the ground and excited state of an impurity. There is no experimental indication where these levels are situated in the forbidden gap. After the impurity is excited then has a radiative or radiationless relaxation to the ground state at the same or at some neighboring impurity site, there is a cutoff of absorption at the minimum energy required for the transition. The minimum energy and the wavelength that it corresponds to within the bandgap for transitions and the corresponding wavelength is called the absorption edge. Light that is of a greater energy than the minimum required for absorption is continuous and mostly constant, up to a certain maximum energy which marks a transition from the bottom of the valence band to the top of the conduction band. There are three possible types of absorption transitions resulting in photoconductivity.

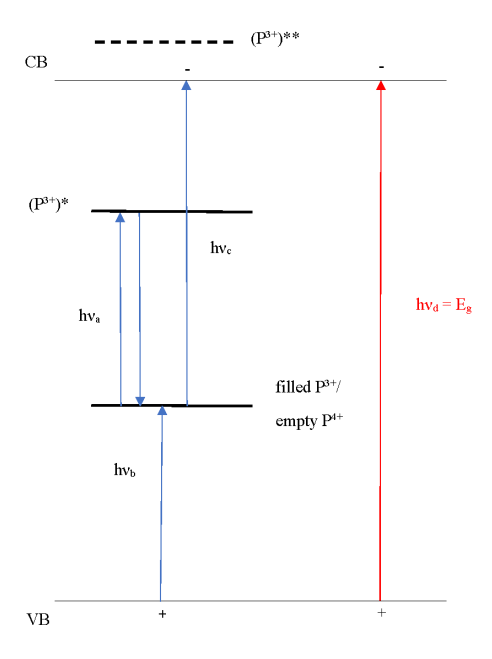


Figure 2.6: Localized and electron transfer processes.

(1) Edge absorption at a photon energy $h\nu_b = h\nu_{CT}$ means that zero absorption up to $h\nu_b$ and increasing absorption beyond that. This transition is for an electron from the filled VB to an empty impurity level, which is known as one of the electron transfer processes, that can be called acceptor-like charge transfer (CT). Along with adding an electron to the impurity ion this transition leaves behind a free hole in the valence band. The VB in insu-

lators is largely made up of anion (ligand) orbitals and therefore this process is also called a "ligand-to-metal" transfer.

- (2) Similarly to edge absorption at the photon energy $h\nu_c = h\nu_{PI}$ an electron is promoted from an impurity level to empty states in the conduction band. This transition effectively ionizes the impurity and is therefore called donor-like charge transfer or photoionization. This also leaves behind a hole localized on the impurity. This transition adds a free electron to the conduction band.
- (3) Edge absorption at a photon energy $h\nu_d$ promotes an electron across the bandgap E_g from the valence band to the conduction band, creating both a free hole and a free electron.

The distinction between acceptor-like charge transfer and donor-like charge transfer are often; but, not only made by means of an electrical measurement that detects freely moving charge carriers in the lattice. Apart from different conductivity mechanisms, the sign of the charge carriers can be determined by the use of the Hall effect. Knowing the electronic configuration of the dopant/impurity allows for the prediction of the probability of the appropriate process based on the absorption spectra only [29].

An analytical tool that can be used to study this is called the Born-Haber cycle: the approach originates from the basic thermodynamics of crystals and is named after the German physicist Max Born and chemist Fritz Haber [30]. The method was originally used to describe the estimation of cohesive energy of ionic lattices. This idea was further developed to find the relationship between photo-ionization and photo-charge transfer energies of the impurity ions in crystals within the basic band structure of solids [31]. The following steps are used when trivalent and tetravalent metal impurity P ions are considered in a host crystal with bandgap E_g .

The charge transfer energy for ionization P^{3+} in the donor-like charge transfer case:

$$P^{3+}(site) \rightarrow P^{3+}(vac)$$
 $E_1 = eV_3$

$$\begin{array}{ll} P^{3+}(vac) \rightarrow P^{4+}(vac) \,+\, e^-(vac) & E_2 = I_4(P) \\ \\ P^{4+}(vac) \rightarrow P^+(site) & E_3 = eV_4 \\ \\ E^-(vac) \rightarrow e^-(CB \ bottom) & E_4 = \chi \\ \\ \text{which yields} \end{array}$$

$$E_{PI} = I_4(P) - e(V_3 - V_4) - \chi \tag{2.2}$$

Here V_i is the total potential for the impurity ion at the crystal site, $I_4(P)$ is free ion fourth ionization potential (in vacuum, (vac)) and χ the electron affinity of the crystal. Below is the charge transfer energy for lowering the valency of P^{4+} , E_{CT} in the acceptor-like charge process:

$$\begin{array}{ll} P^{4+}(\mathrm{site}) \to P^{4+}(\mathrm{vac}) & E_1 = \mathrm{eV}_4 \\ \\ e^-(\mathrm{VB\ top}) \to e^-(\mathrm{CB\ bottom}) & E_2 = E_g \\ \\ e^-(\mathrm{CB\ bottom}) \to e^-(\mathrm{vac}) & E_3 = \chi \\ \\ P^{4+}(\mathrm{vac}) + e^-(\mathrm{vac}) \to P^{3+}(\mathrm{vac}) & E_4 = -\mathrm{I}_4(\mathrm{P}) \\ \\ P^{3+}(\mathrm{vac}) \to P^{3+}(\mathrm{site}) & E_5 = -\mathrm{eV}_3 \\ \\ \text{yielding} \end{array}$$

$$E_{CT} = E_g - I_4(P) + e(V_3 - V_4) + \chi \tag{2.3}$$

The quantities in the equations above ascribe to relaxed thermodynamic states at 0 K (thus corresponding to zero phonon energies) and therefore directly comparing these calculations to experiment is not always straightforward.

$$E_q = E_{PI} + E_{CT} \tag{2.4}$$

Adding E_{PI} to E_{CT} states that the zero phonon energies for the two processes add up to the value of the bandgap of the host crystal E_g [7]. This process is only valid if the mutual interactions between electrons and holes are excluded and therefore the model is not precisely applicable to spectroscopic measurements.

In conclusion the three energy values E_{CB} , E_{VB} , and E_g can be estimated if the other two are known. This can be found from experimental results and the relaxation of a lattice and/or other possible interactions are taken into account in a proper manner.

2.7 Photorefractive Effect

One of the most interesting optical properties of KNbO₃, is the photorefractive effect. It is an interesting nonlinear optical phenomena which depends on the photoconductivity and electro-optic nature of a material. The origin of photorefractives began in 1966 with a study by Ashkin et al [32]. In this research they found that an optically-induced modulation of the index of refraction in samples of (LiNbO₃) and lithium tantalate (LiTaO₃) were observed. In the same year the refractive index modulations had also been observed in potassium tantalate-niobate. Chen [33] published a paper specifically concerning these modulations which in the case of potassium tantalate-niobate occur only in the presence of a laser and a DC electric field. Chen termed the effect "optical damage", given its seemingly destructive effects on the other nonlinear applications to the material. Chen noted in his paper that the observations of the so called optical damage observations could be explained by the accumulation of an electric field produced by charge accumulation around the impinging beam and proposed what would turn out to be a qualitative description of the mechanism of the photorefractive effect.

During the early and middle 1970's there was a growth in the understanding of the mechanisms of the this effect [34]. Amodei determined that the diffusion can be responsible for the effects in LiNbO₃, albeit the model employed was not able to describe the maximum

achievable space charge field [35]. More development in this field came on the theoretical front, made by Glass et al., [36] where asymmetric photocurrents in lithium niobate could explain the result of local asymmetries of Nb-Fe³⁺ distances. More research and developments were made throughout this time period.

The advent of the laser allows us to observe the small magnitude non-linear effects in the perovskite crystal. The orthorhombic KNbO₃ being non centrosymmetric, seems to be an ideal candidate for displaying, second-order nonlinear effects. The lack of center of inversion, combined with a large value of spontaneous electric polarization at room temperature and high packing density units of the polarizable Nb surrounded by the six O atoms that form the oxygen octahedra. This lends the orthorhombic structure of the perovskite to have large values of electro-optic coefficients and nonlinear susceptibilities [9] at room temperature. It was found that the second-order, non-linear opto-electric effect combines with the photoconductive properties in certain perovskites, which include KNbO₃, to yield the phenomenon of photorefractivity.

The photorefractive effect relies on the combination of a material's photoconductive nature along with the material's manifestation of the nonlineaer Pockel's effect. The foundation of this process includes the continual photo-excitation, migration, and eventual trapping of charge carriers. When two beams of appropriate wavelengths are made to interfere within a photorefractive crystal, photo-excitation will occur at the bright fringes of the interference pattern. Depending on the occupation of the states within a given crystal, electrons or electron holes may be excited, in which these states can be described as either donor or acceptor states.

These electrons will travel some average distance with accordance to their lifetime within the material before recombining with the valence band or acceptor states from which they can be re-excited and travel once more. At steady state the distribution of photo-excited electrons and the ionized donors, will generate a spatially modulated distribution of positive and negative charge within the crystal, which is termed as a space-charge field. This space-charge field will be $\frac{\pi}{2}$ radians out of phase with the interference pattern. The refractive index of the material will be locally altered in the presence of a local electric field due to its electro-optic nature.

As the sinusoidal interference pattern is established, electrons excited from donor states in the material create a spatial distribution of excited carriers which matches the interference pattern. This pattern will generate a carrier concentration gradient along which excited carriers will diffuse from the bright fringes to the dark fringes of the interference pattern, leaving behind ionized donor centers.

The photorefractive effect is characterized by a phase shift ϕ between the intensity pattern and the index modulation. In a two-beam coupling experiment this phase shift is responsible for the self-diffraction of the recording beams. There are two different categories of photorefractive materials: inorganic crystals and organic compounds. Inorganic crystals are grown at high temperature, and their composition is imposed by their stoichiometry and crystalline structure. Photorefractive organic compounds are mixtures of several organic molecules displaying specific function to achieve the photorefractive effect. They are mainly composed of a photoconductive polymer matrix that allows charge transport.

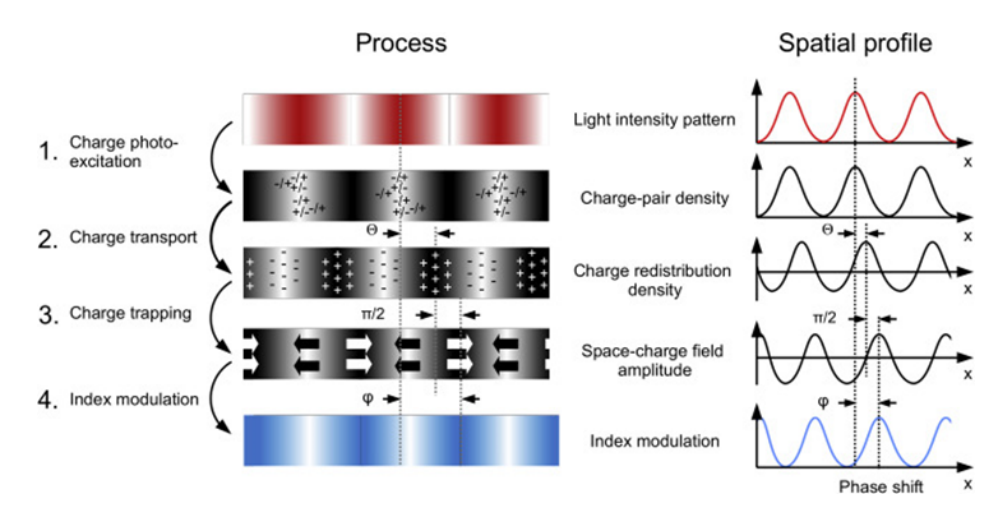


Figure 2.7: Photorefractive process that starts with the intensity distribution of the interference pattern, charge photogeneration, charge transport and distribution after migration and trapping, space-charge field. Finally the index modulation is shown. [37].

However, in some cases with a short time constant for the buildup of the grating or a large energy band gap between the valence and the conduction band, the charge-hopping model, proposed by Hall et al. is most useful [38]. This model uses a mechanism of thermal or photoinduced tunneling of excited states. Both models are aimed at explaining the basis of the mechanism that leads to the creation of the refractive index grating [38].

According to the model derived by Kukhtarev, intervalence impurities are responsible for the photorefractive effect in inorganic crystals, such as KNbO₃, LiTaO₃, Bi₁₂SiO₂₀, etc. As shown in Fig. 2.8, the energy levels of these impurities lie between the band gap of the material.

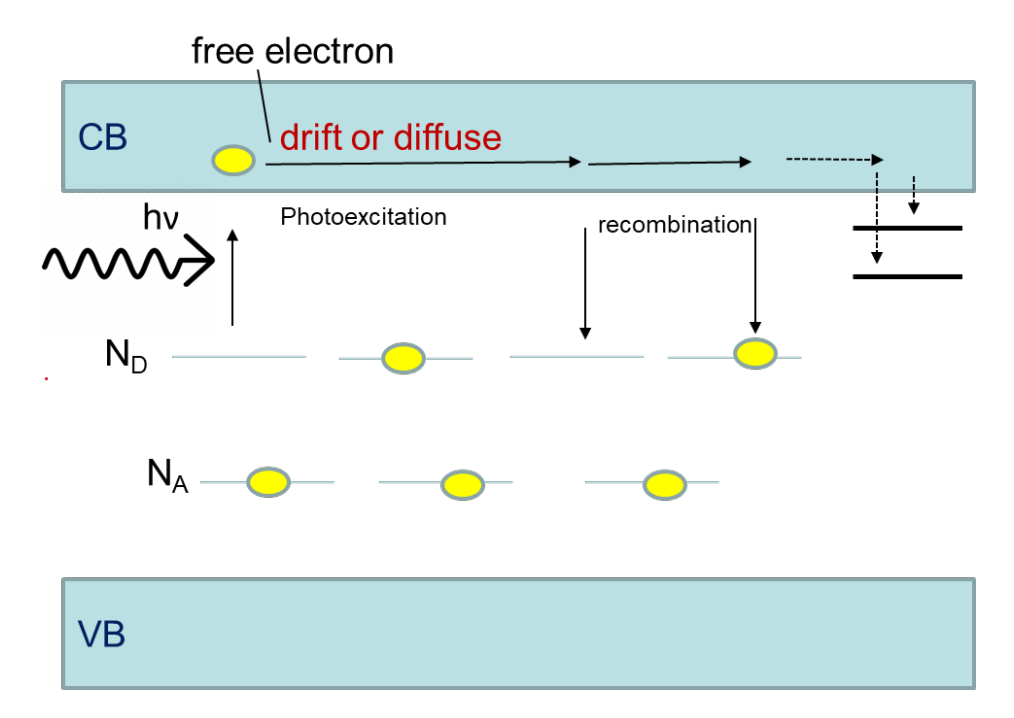


Figure 2.8: A varying index or refraction, electric field, charge distribution, and intensity shifted due to the photorefractive effect.

In the brighter region in Figure 2.8, the electrons are photoexcited from the donor ions into the conduction band, leaving behind donor ions in an increased oxidation state. While the electrons are in the conduction band they can move under the influence of drift or diffusion, and eventually recombine with impurity ions or are trapped by defects in the darker regions. The electrons in the dark regions stay trapped, because photoexcitation is required to liberate them (unless the traps are sufficiently shallow and thermal liberation from the traps can occur). The segregation of electrons in the dark regions and the ionized donors in the bright regions of the crystal generate an internal electric field. Since the electrons and holes are trapped and do not move, the space charge field persists even when the illuminating beams are removed [39]. The periodic field known as a space-charge electric field causes periodic modulations of the refractive index of the material due to the electro-optic effect. The resulting index grating follows the light interference pattern originally imposed on the crystal. The refractive index grating can diffract the incident light beam, to re-create the original beam.

2.8 WILLIAMSON-HALL METHOD

The Williamson-Hall method that was developed by G.K. Williamson and his student W.H. Hall [40]. The Williamson-Hall method is a procedure that is used to analyze stress and strain derived from X-ray diffraction. As maintained by the Williamson-Hall method, the basic calculation for the plot can be performed by using XRD data. Size and inhomogenous strain can broaden the powder diffraction peak. Previous work suggests that the broadening is produced by either lattice strain alone or by lattice strains and small particle size simultaneously. In the Williamson-Hall method, crystal imperfection was considered, and other conditions of the crystal were assumed to spread throughout the crystal. Some of these conditions uniform strain and uniform energy density. The principal relies on the approximation formula for size broadening, β_L , and strain broadening, β_e , vary differently with respect to the Bragg angle, θ .

$$\beta_L = \frac{\kappa \lambda}{L \cos \theta} \tag{2.5}$$

Where λ is the X-ray wavelength.

$$\beta_e = D\epsilon tan\theta \tag{2.6}$$

In terms of the reciprocal lattice the effect of lattice strain is to broaden the reciprocal lattice points to a breadth which varies linearly with the distance from the origin.

One part of the formulae varies as $1/\cos\theta$ and the other as $\tan\theta$. If both contributions are present then their combined effect should be determined by convolution. The simplification of Williamson and Hall is to assume the convolution is either a simple sum or sum of squares. Adding these two equation:

$$\beta = \beta_e + \beta_L = D\epsilon tan\theta + \frac{\kappa\lambda}{Lcos\theta}$$
 (2.7)

If we multiply this equation by $cos\theta$ it can be determined that:

$$\beta cos\theta = D\epsilon sin\theta + \frac{\kappa\lambda}{L} \tag{2.8}$$

This equation can be compared to and used to describe a linear fit, that being the equation y = mx + b. Plotting $\beta cos\theta$ versus $sin\theta$, then using a linear fit it can be found that the slope is the strain component (D ϵ) and the size component can be found using the intercept ($\kappa \lambda/L$). This plot is known as the Williamson-Hall plot and is illustrated schematically in Figure 2.9.

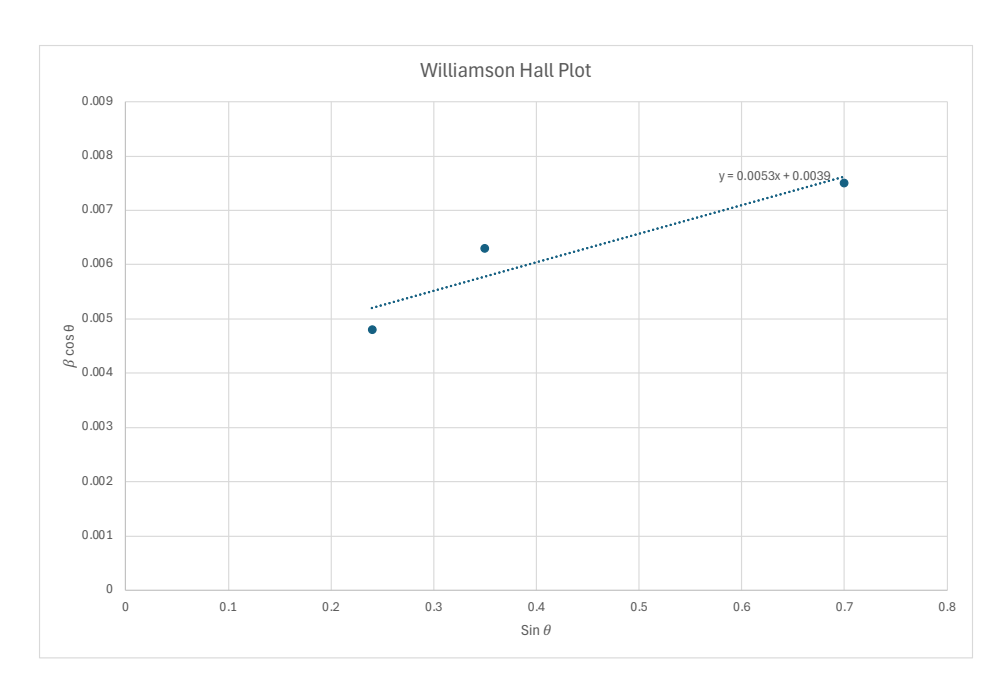


Figure 2.9: A Williamson-Hall plot showing the linear relationship and the slope as an example. The figure shows several reflections as data points. Where the strain component is the slope and the size component comes from the intercept.

Particle size or grain size is used when the size of individual crystals is less than about 100 nm. This is because a real crystalline powder is generally made up of many fine units called crystallites, which can be considered as a single crystal. Figure 2.10 shows a schematic view of particle size to crystallite size.

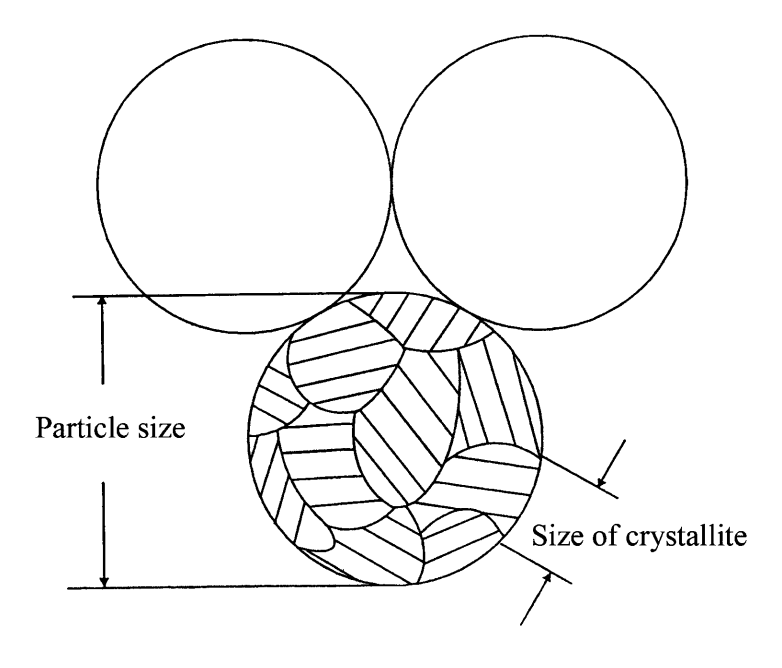


Figure 2.10: Schematic view of the Size of crystallite in reference to that of Particle Size

However, the size of crystallites may be the same as that of grain size in some cases, but they have different physical qualities. In terms of XRD analysis, the size of crystallites usually refers to the cause of diffraction peak broadening. Uniform distribution in all directions of crystallites in a sample is also required to provide the diffraction peak profile to enable reliable results. If the size of crystallites in a crystalline powder sample becomes small less than 5 nm, the measured diffraction peak profile clearly deviates from that of the

same sample with a standard size 500 nm - 1000 nm in diameter.

There are different ways to calculate crystallite size. One way to do this is to use the Williamson-Hall plot. Within the Williamson-Hall plot the Scherrer equation uses peak broadening to estimate crystallite size, and the instrumental broadening and crystal imperfection related effects were neglected [41]. Crystallite size is a term that refers to the dimensions of individual crystalline regions within a material. This can influence chemical and physical properties significantly. Crystallite size relays information about a few properties a material may possess. Some of these properties are mechanical strength, thermal and electrical conductivity, optical properties in semiconductors and nanomaterials, etc. Understanding the crystallite size helps in fabricating materials for the desired application within many different fields, including materials science, engineering, and nanotechnology. To calculate the crystallite size the Scherrer equation is used.

$$L = \frac{\kappa \lambda}{\beta \cos \theta} \tag{2.9}$$

Where L is the crystallite size perpendicular to the lattice planes and κ is the shape factor which is dependent on the non-instrumental and instrumental factors, however the numerical factor that is normally used is 0.9 [42] [43]. The crystallite shape factor of any polycrystalline material depends on factors such as the influence of defects, microstrain, size and shape.

2.9 Crystal Field Theory

In an independent electron picture the d orbitals of a transition-metal ion are five-fold degenerate in free space. This can accommodate a maximum of ten electrons due to spin degeneracy. Crystal field theory describes the breaking of orbital degeneracy in transition

metal complexes due to the presence of ligands. This may lead to a change in magnetic properties as well as color. When investigating a single transition metal ion the five d-orbitals have the same energy. When ligands approach the metal ion some ions will experience more opposition from the d-orbital electrons than others based on the geometric structure of the molecule. When the transition-metal atom is placed at the center of a perfect octahedron with O^{2-} ions at the vertices valence d-electrons experience different repulsive forces. This depends on the shape of the orbitals they occupy. These interactions create splitting due to the electrostatic environment. The d_{z^2} and $d_{x^2-y^2}$ orbitals have lobes that point directly towards the negative point charges on the O^{2-} anion [44]. These electrons experience a strong Coulombic repulsion. This can be seen in Figure 2.11 below.

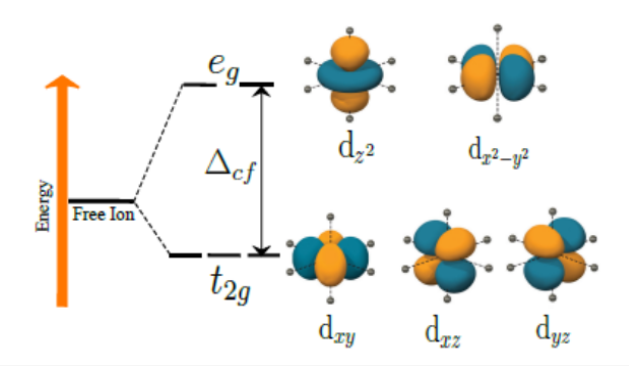


Figure 2.11: The splitting of the d-orbitals of a transition metal due to the d_{z^2} and $d_{x^2-y^2}$ orbitals increase in energy while the, d_{xy} , d_{xz} , and d_{yz} orbitals decrease in energy. The geometry of the two e_g states and three t_{2g} states are shown on the right. [3].

The O^{2-} ions lie on the nodal planes; therefore, the electrons in the d_{xy} , d_{yz} , or d_{xz} orbitals naturally stay away from the anions. This results in an energetically lower state as compared to the d_{z^2} and $d_{x^2-y^2}$. The octahedral complex orbital levels are raised in energy due to the interference with electrons from ligands. There are six ligands attached to the central transition metal in an octahedral complex. The distance that electrons have to move from t_{2g} to e_g dictates the energy that the complex will absorb from an electromagnetic wave. The d_{xy} , d_{yz} , and d_{xz} are energetically lower compared to the d_{z^2} and $d_{x^2-y^2}$. Therefore, the

five degenerate levels split due to the octahedral field into two sets of the higher lying doubly degenerate e_g states and the lower lying triply degenerate t_{2g} states. The designations e_g and t_{2g} are traditional and derive from a symmetry analysis. This phenomenon is referred to as crystal-field splitting and the amount of splitting is denoted by Δ_{cf} .

2.10 TANABE SUGANO

The matrix diagonalization of the Hamiltonian in the strong crystal field approximation for $3d^n$ configuration systems were systematically carried about by Y. Tanabe and S. Sugano in the 1950's. For an octahedral symmetry site, the crystal field of the ligands will lead to a splitting of the energy levels of the possible orbital configurations [45]. The result of their calculations for the $3d^3$ system is shown in Figure 2.12, where Dq/B is a normalized measure of the crystal field strength and E/B proportional to the excitation energy with respect to the ground state. The x-coordinate gives the octahedral field strength and the y-coordinate gives the energy level. The four lowest degenerate energy levels of a 3d³ free ion at the 0 Dq/B limit are described by the term symbols ⁴F, ⁴P, ²G, and ²F. These terms split in the presence of a crystal field. It is important for the lowest transition to be the distinction between the so-called low-field site in which the crystal field is sufficiently low to lead to a quartet state as the lowest excited state. The high field sites where the lowest excited state is a doublet state, i.e. the transition is accompanied by a spin flip and thus highly forbidden (resulting in relaxation times that can lie in the millisecond range). The Tanabe-Sugano diagram gives energy levels of the excited states relative to that of the ⁴A₂ ground state [6]. As the ligand field strength increases transitions can occur from the t_{2g} level to the e_g level depending on the ligand environment.

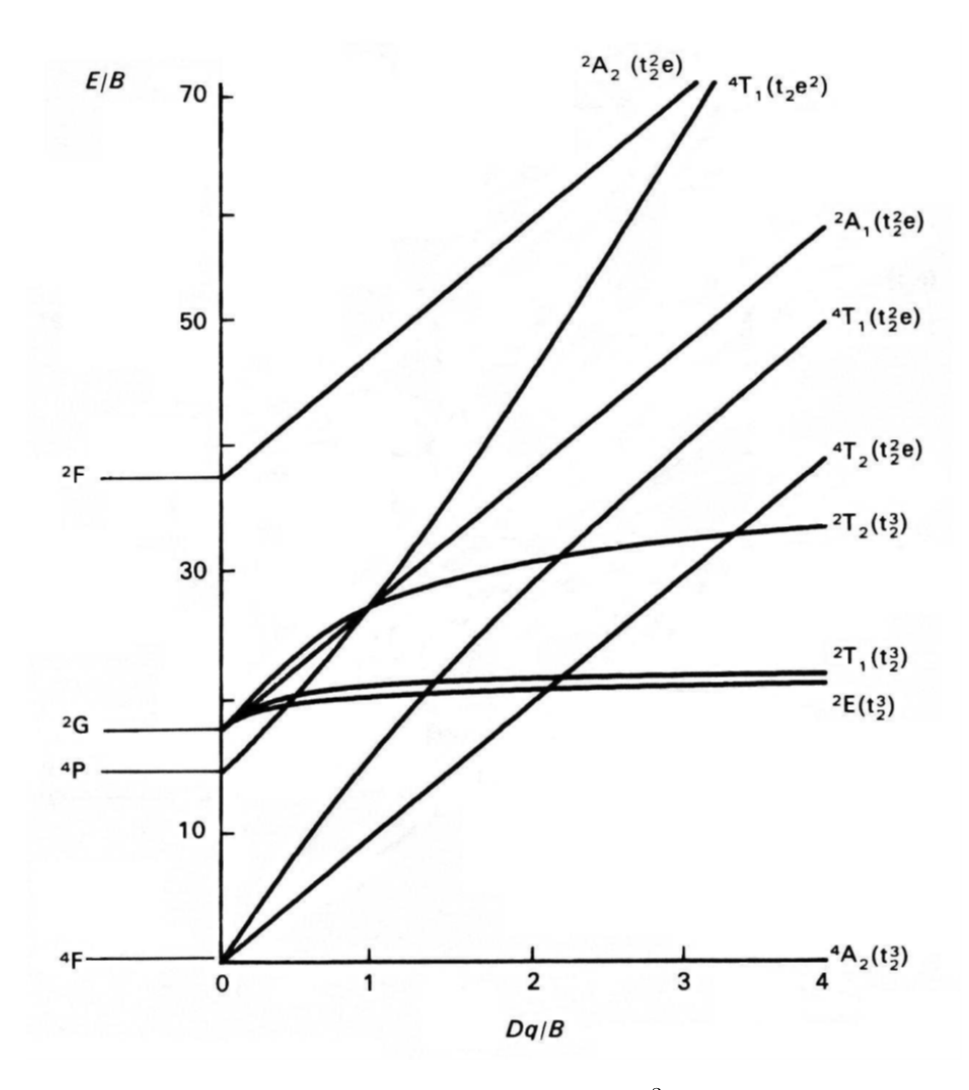


Figure 2.12: Tanabe-Sugano energy level diagram for $3d^3$ system. Diagram obtained from Henderson and Imbusch [6].

2.11 Madelung Energy

Crystalline solids are basically classified into five classes: molecular, ionic, covalent, metallic, and hydrogen bonded. A crystal consists of a periodic array of atoms. This can be defined mathematically as a space lattice shown below [46].

$$\vec{r} = n_1 \vec{a_1} + n_2 \vec{a_2} + n_3 \vec{a_3} \tag{2.10}$$

Where n_1 , n_2 , n_3 are integers and $\vec{a_1}$, $\vec{a_2}$, $\vec{a_3}$ are said to be the primitive vectors. This discussion will cover only ionic crystals. Ionic crystals are made up of positive and negative ions. The ionic bond comes from the electrostatic interaction of oppositely charged ions. The idealized model of an ionic crystal supposes that the constituents are positive and negative ions with charges which are multiples of the electronic charge therefore the charge is distributed with spherical symmetry on each ion. The energy from ionic crystals involves individual ions within a crystal lattice structure rather than individual atoms.

The long-range interaction between ions with +/- charge is the electrostatic interaction +/- q^2/r is repulsive between ions of the same charge and attractive between ions of unlike charges. The arrangement of ionic crystals gives the strongest attractive interaction compatible with the repulsive interaction at short distances between ion cores. The structure is determined by the optimal use of space for the ionic raidii of atoms within the lattice structure in question. The Coulomb attraction between oppositely charge ions should be greater than the repulsion between ions of same sign. The essential factor in minimum separation is the ionic radii. If ions were to approach closer, a strong overlap between the ionic electron clouds would occur. For fully occupied electron shells the Pauli exclusion principle would require that higher lying antibonding orbitals are occupied. This should lead to a steep increase in the energy and therefore a strong repulsion [47]. The attractive Coulomb contribution to the ionic bond can be described as a sum over the Coulomb potentials ion sites.

For the potential energy between two singly charged ions i and j at a separation r_{ij} can be written as

$$\phi_{ij} = \pm \frac{e^2}{r_{ij}} + \frac{\lambda}{r_{ij}^n} \tag{2.11}$$

the second term is a description of the repulsion between the two electron clouds. The + sign is to be taken for like charges and the – sign for unlike charges. λ and n are constants to be determined from observed values of the lattice constant of compressibility. The value

of ϕ doesn't depend on whether the reference ion i is a positive or a negative ion. The sum can be made to converge rapidly; its value will not depend on the location of the reference ion within the crystal as long as it is not near the surface. Neglecting surface effects, the total lattice energy U_{tot} of a crystal composed of 2N ions can be written by the following equation.



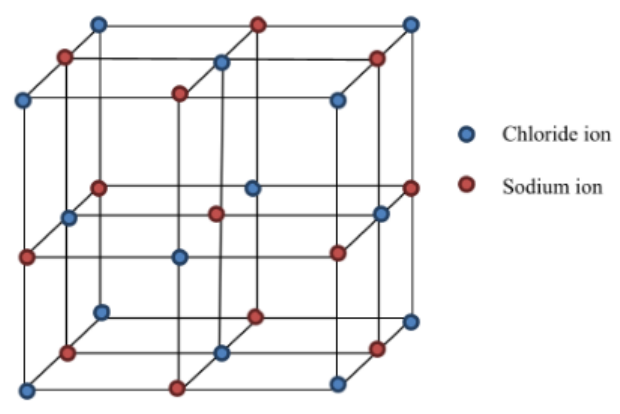


Figure 2.13: NaCl Image obtained from Gelest [37].

Sodium chloride crystallizes into the structure shown in Figure 2.12. Here, N is used rather than 2N since taking the total lattice energy interactions per each pair must be counted only once. If $r_{ij} = p_{ij}R$, where R is the nearest neighbor distance in the crystal then Equation 2.10 can be written as,

$$\phi_{ij} = \pm \frac{e^2}{p_{ij}R} + \frac{\lambda}{p_{ij}^n R^n} \tag{2.13}$$

$$\phi = \frac{\lambda A_n}{R^n} - \frac{\alpha e^2}{R} \tag{2.14}$$

Where,

$$A_n = \Sigma_j' \frac{1}{p_{ij}^n} \tag{2.15}$$

and

$$\alpha = \Sigma_j' \frac{1}{p_{ij}} \tag{2.16}$$

Here, the quantity α is known as the *Madelung Constant* and is a property of the crystal lattice. The Madelung constant is of central importance in the theory of ionic crystals. The first calculation of the coulomb energy constant α was made by Erwin Madelung. The Madelung constant is calculated using an infinite line series of nearest-neighbor distances for an infinite line of ions of alternating signs in one dimension. In three dimensions the series presents a greater difficulty [46]. It is not possible to write down the successive terms in the series by casual inspection. More to the point, the series will not converge unless the successive terms in the series are arranged so that the contributions from the positive and negative terms nearly cancel. A powerful general method for lattice sum calculations was developed by Paul Peter Ewald. Computers are more readily used for this calculation.

2.12 VESTA PROGRAM

Considering a lattice made up of ions with positive or negative charges and assuming that the ions are spherical; the Ewald summation is an excellent technique for calculating electrostatic interactions in a periodic system. Calculating the electrostatic potential experience by one ion in the presence of all the other ions in the crystal can be problematic. The problem with calculating the Coulomb sum is the 1/r behavior. This means that the Coloumb potential is singular at each particle position and 1/r potential is very slowly decaying. The solution is to compute the total potential at an ion as the sum of two distinct but related potentials. These potentials can be written as two terms.

$$\Phi(r_i) = \phi_S(r_i) + \phi_L(r_i) \tag{2.17}$$

 $\phi_S(\mathbf{r}_i)$ is the short range term that converges quickly in real space while $\phi_L(\mathbf{r}_i)$ is the long range term that converges in Fourier space where the sums are converted into two exponentially converging sums.

The reason that many compounds would take on the perovskite structure type ABO₃ has been explained by ion-packing and tolerance factor determined by Goldshmidt [48]. However, lattice and valence stabilities should be more related to thermodynamic energy and originate from thermodynamic principles rather than numerical geometrical parameters. Van Gool and Piken have shown that crystal chemistry and thermodynamic energy of ionic solids are reflected into Madelung electrostatic potential [49]. The present work is written by the use of the Madelung lattice energy and site potentials based upon data calculated using VESTA program and the crystallographic, structural data from Hewat et. al. [8]. Ionic solids are stabilized due to the gain in lattice energy that is reflected in the Madelung electrostatic potential (E_{Mad}). The total internal energy of ionic solids may be expressed as

$$E = E_{Mad} + E_N \tag{2.18}$$

Where E_{Mad} is the Madelung electrostatic potential energy and E_N is the combination of all other energies: repulsive, zero point, crystal stabilization, vibrational, van der Waals and covalent energies. In this research the development of the Madelung electrostatic potential and lattice site potential were completed only for KNbO₃ dope with Cr^{3+} . The lattice stability and valence stability are understood from the Madelung electrostatic potential viewpoint and valence stability directly related to the lattice site potential. Based on this idea, the Madelung energy is used to estimate the position of the trivalent chromium impurity within the KNbO₃ crystal structure and by using the ionization energy to remove one electron from trivalent chromium.

2.13 X-RAY DIFFRACTION

Crystal structures of organic and inorganic compounds have been explored using X-ray diffraction (XRD). In 1912 von Laue discovered that probing using X-ray radiation on the order of angstroms will give detailed information on the structures of crytals [42]. The discovery of XRD has been considered as the principal method for determining the arrangement of atoms in minerals, metals, semiconductors, as well as all kinds of inorganic, organic and biological molecules. Single crystal XRD analysis has become one of the most important authoritative methods as it facilitates direct visualization of the internal structure; which in turn helps improve and expand our knowledge understanding the microstructures and properties of materials.

An X-ray diffractometer is a precision instrument with two axes (ω and 2θ) of independent rotation. This equipment allows one to obtain the intensity data of a diffracted X-ray beam as a function of an angle to satisfy Bragg's law under the condition of X-rays of known wavelength. The design basics of a diffractometer are illustrated in Figure 2.13 [50]. There are three components of an X-ray diffractometer; X-ray source, sample holder and detector which lie on the circumference of a circle known as the focusing circle. When the position of the X-ray source is fixed and the detector is attached on the 2θ -axis, a powder sample in the flat-plate form is usually set on the ω -axis corresponding to the center of the diffractometer. The focal spot on the target of the X-ray tube is set to be parallel to the diffractometer ω -axis. A flat plate sample is used in order to take advantage of the focusing geometry for effectively collecting the intensity of weak diffracted beams. During the course of measurements the 2θ -axis rotates two times as much as the ω -axis; therefore, it is frequently called the two-theta scan. This experimental condition is used to maintain the angle between the plane of the sample and direction of the incident X-ray beam which is equal to the direction of the diffracted beam with reference to the direction of propagation of the incident X-ray beam.

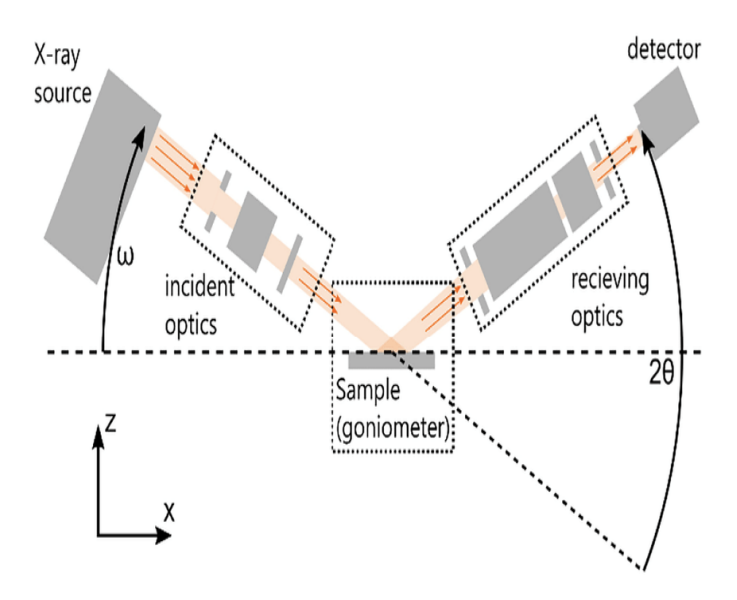


Figure 2.14: Essential components of an X-ray Diffractometer. Diagram obtained from G. Harrington and J. Santiso [51].

The spacings and atomic arrangements of solids have been directly obtained from XRD characterizations. XRD is the study used to determine the structure of potassium niobate samples, rather to identify the phase of the samples. The crystal structures of potassium niobate and other ferroelectrics have been rigorously determined by A. W. Hewat et al by Neutron scattering experiments in the 1970's [2].

The instrumentation used in this research consists of a monochromatic X-ray source and a detector, each mounted on its own rotatable table. The sample is mounted at the common rotation axis of the two tables. Measurements are done by scanning the sample which involve sweeping or rotating the detector over an angular area of interest; then recording the X-ray signal intensity as a function of the angle of the detector referenced to the collimated incident beam. The X-ray is detected wherever the Bragg condition is satisfied. The Bragg condition is met when the path differences of the reflected collimated x-ray beams from successive planes of ions are an integer multiple of its wavelength, resulting in constructive interference. Therefore, the constructive interference is a function of the angle of incidence and the distance between successive ion planes. Similarly to optical diffraction gratings, the large number of ionic centers and planes produce sharp XRD peaks.

The X-ray powder method is used in taking an XRD spectroscopy of the sol gel samples in these experiments. Samples were prepared by cleaning the spatula and the slide microscope slide. Then place the sample in a quartz square well using a microscope slide to spread and flatten the sample on the square well. The square well is then placed into a sample puck and is mounted in the Bruker D8 Advance X-ray Diffractometer which uses a Co K α radiation source with a wavelength, $\lambda = 1.79$ Å. This was a different X-ray source than Tanaka et. al. used. Tanaka et. al. used an X-ray source of Cu K α that has a wavelength $\lambda = 1.54$ Å. X-rays with longer wavelength allow for observation of low-angle peaks that are not observable using shorter wavelengths. This provides better peak separation.

CHAPTER 3

SOL GEL PROCESS

3.1 Introduction

The motivation for the present study originates from interest in photorefractive materials in the near IR. Through computational simulation it appears that $KNbO_3$ doped with Cr^{3+} is a good candidate. Due to the volatility of K_2O , it could be preventing the crystallization of single-phase $KNbO_3$. The alternative method to fabricate $KNbO_3$ used in this research project was the sol gel process.

3.2 Brief History

Sol gel processing is a technique that was first done in 1845 in France. M. Ebelmen at the "Manufacture de Ce'ramiques de Sevres" was the first to synthesize silica gels. However, this processing technique has experienced an important developmental stage, after the publication of the first edition of the book by Kluwer. The sol gel process is essentially a wet chemical approach for producing solid inorganic oxides. The process involves the transformation of a non-viscous, colloidal suspension (sol) into a viscous gel that will form to the shape of its container. Drying and heat treating of the gel produce a ceramic material at low temperatures. The fabricated ceramic materials can range from nanocrystallites, to ceramic or glass fibers, to optical grade thin films, highly porous aerogels, and inorganic membranes. The sol gel technique offers one of the most versatile, simplest, and inexpensive modes of fabrication ceramics and glass materials. Figure 3.1 shows a flowchart of possible routes in the synthesis of materials made using the sol gel technique.

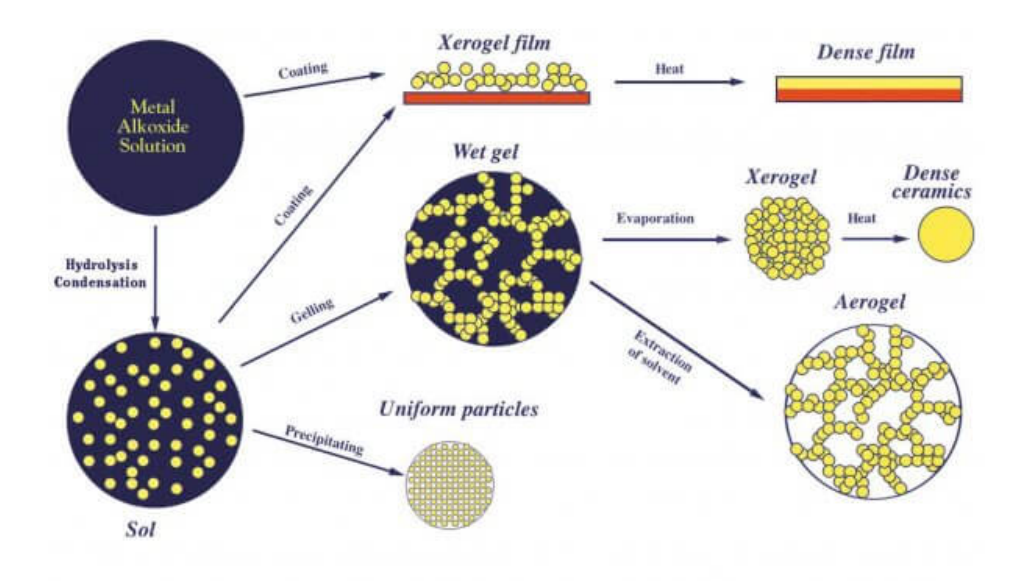


Figure 3.1: Sol gel process involves precursor materials that are processed through several sol gel synthesis routes. Image obtained from Gelest [37].

A sol gel converts monomers into a colloidal solution. A colloid is a suspension where the dispersed phase is small enough that gravitational forces are negligible. The interactions are caused mostly by short range forces such as van der Waals attraction and surface charges. The colloidal suspension which is called a sol includes the solid particles in a liquid. Polymerization continues during gelation as hydrolysis and condensation reactions occur on different sites of the molecules which in turn results into growth in three dimensions and spans throughout the container; the precursor materials reside in side The viscosity of the solution increases dramatically to form a "gel". The colloid is used to generate polymers or particles from which a ceramic can be made at lower temperatures [52]. The basic process includes the following: hydrolysis, condensation, gelation, aging, drying and densification. In this project instead of hydrolysis a reflux method was used in the synthesis process. This method was used to break the double metal bonds Niobium pentaethoxide and potassium ethoxide in a more controlled manner. The reflux method is a sol gel processing technique

that works basically the same as a distillation process. The precursor materials are heated in a solvent such as 2-methoxyalcohol in a reflux chamber as shown in Figure 3.3. As the precursor materials and the solvent are heated, the solution changes to the gas phase. As the gas flows to the top of the reflux chamber it is cooled by the condenser on top of the chamber. The condenser acts as a cooling system where constant flowing water is used as the coolant. Once the gas solution meets the condenser it cools and changes back to the liquid phase in which the solution falls back into the chamber and is reheated. Over a period of time the solution is heated; this process repeats and the double meal bonds eventually are broken.

3.3 Sol Gel Process Using the Reflux Method

A double metal alkoxide solution of potassium ethoxide and niobium pentaethoxide were refluxed under an argon gas for an extended period of time. This additional step allows greater flexibility in controlling the ratios of the two metals. Since alkoxides are very sensitive to moisture, the process was done in a dry box that was purged with argon gas. Figure 3.2 shows the skeletal formula for the reflux process of the double metal alkoxide. The potassium ethoxide and niobium pentaethoxide were refluxed in 2-methoxyethanol. The following equation shows the net equation of the sol gel process before the sintering steps. $CH_3CH_2OK + Nb_5 + (OCH_2CH_3)_5 \rightarrow KNb(OCH_2CH_3)_6$ Reflux begins when 2-methoxyethanol is heated to $80^{\circ}C$ and a dry powder potassium ethoxide is added.

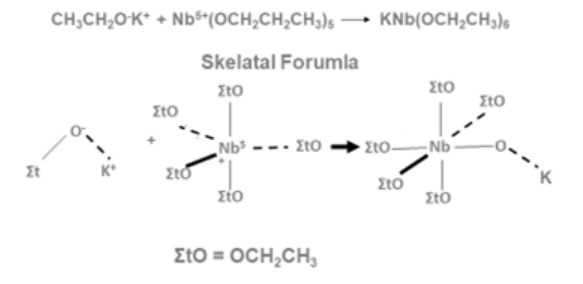


Figure 3.2: The Skelatal Formula of the reflux reaction of potassium ethoxide and niobium pentaethoxide.



Figure 3.3: The reflux chamber used in this project. The condenser is the clear tube on top with the two hoses connected for a constant flow of water.

Chapter 4

Techniques for Characterizing CR^{3+} and the Host Crystal

4.1 Theoretical Results of the Photoexcitation Energy of Cr^{3+} Within $KNBO_3$ Using the Nearest Neighbor Madelung Potential

The Madelung potential was used in the form of the nearest neighbor potential energies at the niobium site replaced with trivalent chromium. This method is used to show that Cr^{3+} doped KNbO₃ is possibly photorefractive in the NIR region. Similarly in prior theoretical work [3] [12] the Niobium site was replaced with a chromium ion Cr^{3+} due to the general thought that dopants with +3 charge states have an atomic radii closer to the of Nb⁵⁺ and should minmize the stress on the unit cell. Given this assumption, an oxygen ion (O^{2-}) is removed which would presumably bind the dopant to attain the +3 charge. With the likelihood of this charge compensation being the case it has been found that Cr^{3+} is a good candidate as a dopant for KNbO₃ that is photorefractive in the NIR. Figure 4.1 is an illustration of expected energy transistions with the use of Madelung nearest neighbor calculations. In this figure, the green arrow indicates the ionization of a free Cr^{3+} ion (I_{Cr}) and E_{PI} indicates the ionization energies of the trivalent chromium site. Here, the photoionization energy depends on ionization potential of a free ion located below the conduction band (CB).

The Madelung potential at a certain site can be calculated using the equation below. Here $V_{M(i)}$ is the Madelung potential at site i, q_j is the charge of atom j and \mathbf{r}_{ij} representing the average distance from the atom i to the jth atom and including atomic radii to give center to center distance of each ion in question. After finding the $\Sigma_i V_{M(i)}$, that negative potential energy is then multiplied by the charge q which can also be seen in Figure 4.1. That charge q is the charge of the Cr^{3+} . This negative potential energy of $q\sigma_i V_{M(i)}$ is added to the ionization energy of a free Cr^{3+} ion. This results in E_{calc} . E_{calc} represents the energy level that the Cr^{3+} impurity lies within the host lattice.

$$V_{M(i)} = \sum_{i} \frac{q_j}{4\pi\epsilon r_{ij}} \tag{4.1}$$

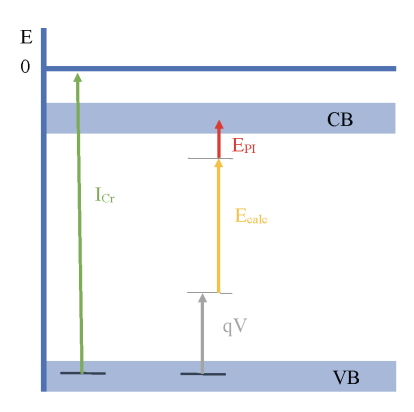


Figure 4.1: Nearest Neighbor potential energy level diagram showing the photoexcitation energy level of $\rm Cr^{3+}$ impurity site.

In the Figure 4.1 charge q is the charge of the Cr^{3+} ion which would be

$$q = 3(e) \tag{4.2}$$

where the 3 indicates the plus 3 charge of the chromium cation that looses an electron in the donor process and the e is the coulombic charge of an electron (1.602 X 10^{-19} C). This is due to the need to find the nearest neighbor potential of the crystal before the Cr^{3+} ion is ionized and becomes Cr^{4+} . Each Madelung nearest neighbor site potential was then added together and multiplied by the charge of the chromium ion.

The nearest neighbor site potentials were found by calculating the ionic center to center distance from each adjacent 3-D positions of the K^{1+} , the O_{β}^{2-} , and the O_{γ}^{2-} ions to the Cr^{3+} . These distances were also added to the ionic radii of each atom. This was used to find the total average r_{ij} distance and to find the nearest neighbor site potential for each ion with respect to the Cr^{3+} ion.

Table 4.1. Lattice cooridnates of ions used in Nearest Neighbor Site Potential for Madelung Potential.

Lattice coordinates for the ions in the ${\rm KNbO_3:Cr^{3+}}$ unit cell.

K^{1+}	at	[0, 0, 0.017]
~ -	at	[0.5,0,0.5]
0^{2-}_{β} 0^{2-}_{γ}	at	$[0.5,\ 0.254,\ 0.285]$
${\rm O}^{2-}{}_{\gamma}$	at	[0.5, 0.746, 0.285]

Table 4.2. Phase and Structural Parameters.

Structural Parameters found experimentally by Hewat et. Al.

Phase	Structural Parameters (Experimental)
Orthorhombic	$egin{array}{ll} { m a} = 3.9710 \; { m \AA} \ { m b} = 5.6920 \; { m \AA} \ { m c} = 5.7190 \; { m \AA} \ { m lpha} = { m eta} = { m \gamma} = 90^{\circ} \end{array}$

Table 4.3. Ionic Radii of Ions for Nearest Neighbor Site Potential.

Ionic Radii					
Ion	Ionic Radii	variable			
K^{1+} Cr^{3+} O^{2-}	1.51 Å 0.62 Å 1.40 Å	K _{ionicradii} Cr _{ionicradii} O _{ionicradii}			

Using the data from Tables 4.1, .4.2, and 4.3 the nearest neighbor potential was found using the following equations. The data in the tables comes from the work of Hewat et. al [2] and from the CRC Handbook of Chemistry and Physics, [53].

For the K^{1+} to the Cr^{3+} , r_{ij} distance used

$$r_{CrtoK} = \sqrt{((0-0.5)a)^2 + ((0-0)b)^2 + ((0.017-0.5)c)^2} + K_{ionicradii} + Cr_{ionicradii}$$
 (4.3)

For the ${\rm O}_{\beta}{}^{2-}$ to the ${\rm Cr}^{3+},$ ${\rm r}_{ij}$ distance used

$$r_{CrtoK} = \sqrt{((0-0.5)a)^2 + ((0-0)b)^2 + ((0.017-0.5)c)^2} + K_{ionicradii} + Cr_{ionicradii}$$
 (4.4)

For the ${\rm O}_{\gamma}^{\,2-}$ to the ${\rm Cr}^{3+},\,{\rm r}_{ij}$ distance used

$$r_{CrtoO_{\gamma}} = \sqrt{((0.5 - 0.5)a)^2 + ((0.746 - 0)b)^2 + ((0.285 - 0.5)c)^2} + O_{ionicradii} + Cr_{ionicradii}$$
(4.5)

These average distances are used to find the nearest neighbor Madelung potential which is multiplied by charge, q, which is the charge of the Cr^{3+} mentioned earlier. Each nearest neighbor Madelung potential energy charge comes from K^{1+} ion and the two O^{2-} where the charge of an electron, e is multiplied by a 1 and a -2 for each of the potential energies of the potassium and oxygen ions respectively.

Figure 4.1 shows the use of the nearest neighbor Madelung potential, ΣV_M times the charge of the chromium ion q, to first find E_{calc} and to find the ionization energy E_{PI} of the chromium ion within the host KNbO₃ lattice.

Adding the Ionization energy of a free Cr³⁺ to the negative nearest neighbor Madelung potential we find that

$$E_{calc} = I_{Cr} + -q\Sigma_i V_i \tag{4.6}$$

where E_{calc} is 3.06 eV. This information is used to find where the impurity energy level lies below the conduction band (CB) of the host KNbO₃ lattice. Subtracting E_{calc} from the known experimental bandgap of KNbO₃ will give information to where the energy level at which the Cr^{3+} impurity lies with respect to the CB [54] [55].

$$E_{PI} = 3.3eV - E_{calc} \tag{4.7}$$

 E_{PI} is found to be 0.24 eV which suggest that the Cr^{3+} impurity within the KNbO₃ host would lie 0.24 eV below the CB and would also suggest that the photoexcitation energy for the Cr^{3+} ion would be close to the near infrared electromagnetic energy level. This would be in agreement with what was previously found in other theoretical studies.

4.2 Theoretical Results of the Activation Energy Cr^{3+} Within KNbO $_3$ Using VESTA Program to Calculate Madelung Potential

The calculation on pure KNbO₃ are presented in this section. The present work is using the Madelung lattice energy based upon recent data calculated using VESTA program [8]. The Madelung Potential is a powerful method to find the binding energy of ionic crystal. KNbO₃ has a high symmetry cubic phase and a is paraelectric in nature at temperatures above 435 °C. In the cubic phase KNbO₃ the potassium, K, and the Niobium, Nb, atoms are located at the corner and body center respectively, and the Oxygen, O, atoms are located at the face centers of the unit cell. As the temperature is lowered, zone center and zone boundary distortions along [100], [110] and [111] directions produces three phase transitions. These phase transitions happen as the temperature goes below 435 °C. The first transition is from the cubic to the tetragonal, the next transition is from tetragonal to orthorhombic below 235 °C and then from orthorhombic to rhombohedral below -10 °C. Each of these phases reduces symmetry making them ferroelectric with Nb atom at the body center being displaced with respect to the O octahedral cage surrounding it. This yields a non-zero spontaneous electric polarization that can be reversed with the application of an external electric field.

Above the phase transition temperature of 435 °C, KNbO₃ has the aristotype cubic perovskite structure, with K at (000), Nb at ($\frac{1}{2}$ $\frac{1}{2}$ $\frac{1}{2}$) and O at ($\frac{1}{2}$ $\frac{1}{2}$ 0), ($\frac{1}{2}$ 0 $\frac{1}{2}$) and (0 $\frac{1}{2}$ $\frac{1}{2}$)
on a unit cell of around 4 Å. Which is where all phase transitions displacements are based.
The origin is chosen by requirement that the center of mass cannot move in the transition.
It was chosen by Hewatt et al. that Δ Nb remains fixed while the other terms are displaced.
The structural parameters, including the lattice constants as well as the magnitude and direction of the displacements for the different atoms in the KNbO₃ lattice used in this work
were experimentally evaluated by Hewat et. al. The values are reported in the table below. The Δ symbols in the table refer to the net displacement expressed in terms of lattice
coordinates of the associated atom from its corresponding position in the cubic aristotype
along the directions specified in the Δ values. In the experiments, the assumption that the

center of mass cannot move during a phase transition fixes the displacements of Nb atom/s in terms of the other atoms. The experimental data found by Hewat et. al., is incorporated in the present theoretical calculations by keeping the Nb atom/s in each unit cell fixed in position during structural relaxation. Therefore $\Delta(Nb)$ are reported to be zero. The three oxygen atoms at face centers of the high symmetry cubic unit cell which are equivalent in the cubic phase and are distinguished as O_{α} , O_{β} , and O_{γ} . They will not be identical in the lower symmetry phases. The data for the orthorhombic phase is important to this work and is reported in Table 4.4.

Table 4.4. Lattice coordinates of the atoms in the KNbO₃ base cell.

First set of lattice coordinates for the atoms in the KNbO_3 base cell

K	at	$[0, 0, \Delta_z(\mathrm{K})]$
Nb	at	$[0.5,0,0.5+\Delta_z({ m Nb})]$
$O\alpha$	at	$[0,0,0.5+\Delta_z({\rm O}_\alpha)]$
O_{β}	at	$[0.5, 0.25 + \Delta_y({\rm O}_\beta), 0.25 + \Delta_z({\rm O}_\beta)]$
O_{γ}	at	$[0.5, 0.75$ - $\Delta_y({ m O}_eta), 0.25 + \Delta_z({ m O}_eta)]$

Second set of lattice coordinates for the atoms in the KNbO₃ base cell

The conventional unit cell of the orthorhombic phase has 10 atoms. There are two formulas units for each $KNbO_3$ and is denoted as the 1 x 1 x 1 base cell. The lattice coordinates of the atoms in this cell are given in Table 4.4.

The parameter $\Delta_z(\text{Nb})$ is determined by the requirement that the center of mass is unmoved by these displacements. The room temperature phase is a result of zone boundary distortions of the high symmetry cubic unit cell leading to cell doubling. Using the experimentation done by Hewat et al., the three optimized lattice vectors for the pure orthorhombic $1 \times 1 \times 1 \text{ KNbO}_3$ cell computed here using the VESTA program are a = 3.9710 Å, b = 5.6920 Å, and c = 5.7190 Å, where vectors are written relative to the high symmetry cubic phase as can be seen in Table 4.5. The experimental data used to build the $1 \times 1 \times 1$ supercell in the VESTA program was used to find the Madelung potential energy of KNbO₃. This potential energy is the main contributor to the binding energy of ionic crystals.

Table 4.5. Phase and Structural Parameters.

First set of lattice coordinates for the atoms in the KNbO ₃ base cell				
Phase	Structural Parameters (Experimental)			
Orthorhombic	$egin{array}{l} \mathrm{a} = 3.9710 \; \mathrm{\mathring{A}} \ \mathrm{b} = 5.6920 \; \mathrm{\mathring{A}} \ \mathrm{c} = 5.7190 \; \mathrm{\mathring{A}} \ \Delta_z(\mathrm{K}) = 0.017 \ \Delta_z(\mathrm{Nb}) = 0.000 \ \Delta_z(\mathrm{O}_lpha) = 0.021 \ \Delta_z(\mathrm{O}_eta) = 0.0035 \ \Delta_y(\mathrm{O}_eta) = 0.004 \end{array}$			

Values used for Madelung Energy using VESTA are as follows, $\alpha = \beta = \gamma = 90^{\circ}$ Volume = 129.26 Å³ found in JCPDS-71-0946 data and Mohua et. al. In VESTA the spheres represent different atoms; but do not necessarily corresponding to their ionic radii. The purple spheres represent Potassium atoms, the green spheres represent Niobium atoms and the red spheres represent oxygen atoms. Using VESTA, the Madelung electrostatic potential for KNbO₃ has been calculated. Similarly, prior theoretical studies have replaced the Niobium site with a Chromium ion (Cr³⁺) to reduce stress on the unit cell and removed an Oxygen ion (O²⁻) for charge compensation within the unit cell. The nearest neighbor O²⁻ was removed in the Madelung calculation that was similarly used in prior theoretical work where the O²⁻ ion was removed in the coordinated vacancy model [11]. In this research the O²⁻ nearest neighbor removed was the O_{α} ion within the VESTA program to find the Madelung potential energy. This model can be seen in the Figure 4.2.

The Madelung electrostatic potential has been calculated using first principle calculation software packages. VESTA has been used to calculate the Madelung electrostatic potential directly from the known crystal structure of KNbO₃ and from experimental research of Hewat et al. The Madelung electrostatic potential obtained from VESTA has the unit of electron

volts (eV) [8]. In VESTA lattice site potentials ϕ_i and Madelung electrostatic potential E_M of a given structure is calculated using the equations below.

$$\phi_i = \Sigma_j \frac{Z_j}{4\pi\epsilon_0 l_{ij}} \tag{4.8}$$

Where Z_j is valence of ion j, ϵ_0 is permittivity of free space in a vacuum and l_{ij} is the distance between ions i and j.

$$E_M = \frac{1}{2} \Sigma_i \phi_i Z_i W_i \tag{4.9}$$

where

$$W_i = \frac{(occupancy)x(number of equivalent position)}{number of general equivalent positions}$$
(4.10)

For structures with fixed atomic positions, such as NaCl, the lattice site potential ϕ_j for each site in the crystal structure is inversely proportional to the characteristic length. Yoshimura et al. noted that lattice site potential ϕ_j , the Madelung constant and Madelung electrostatic potential E_M varies with valence states.

All calculations for the Madelung electrostatic potential were performed using VESTA employing the radius of ionic sphere of 1.6 Åand reciprocal space range of 4 Å⁻¹. The model for the doped host material, KNbO₃ used in the presented calculations was obtained by using the pure orthorhombic conventional 1 x 1 x 1 unit cell, using data from Hewat et. al, which is shown in Figure 4.2.

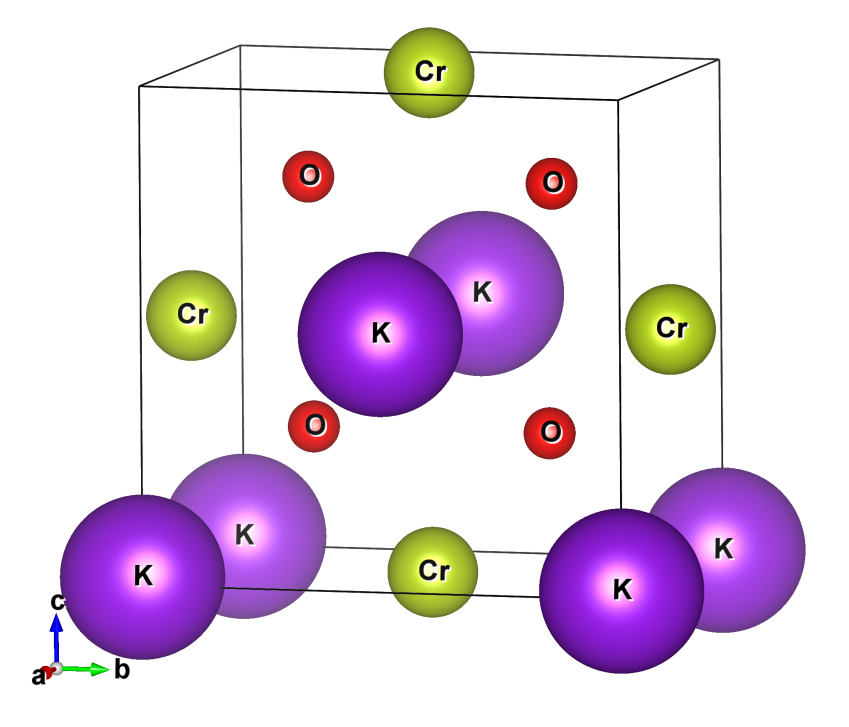


Figure 4.2: Unit cell 3-D picture from VESTA, used in calculations of the Madelung Energy.

Similarly the conventional 1 x 1 x 1 unit cell can be expanded two fold along the [100], [010], and [001] directions and can be referred to as a 2 x 2 x 2 supercell in VESTA. This shows that the unit cell built in VESTA can be expanded in the same way giving the same appearance as the 2 x 2 x 2 supercell used in previous theoretical work with a side-by-side view in Figure 4.3.

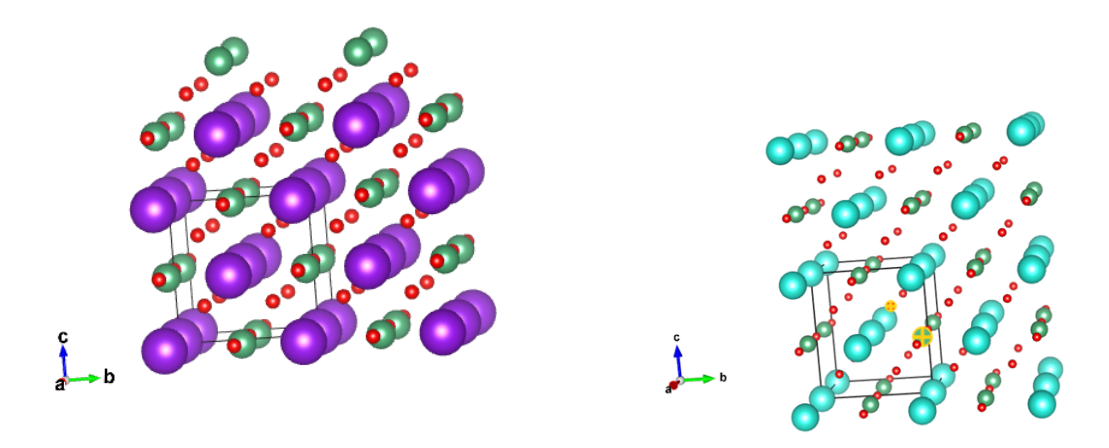


Figure 4.3: Side-by-Side view of KNbO₃ supercells

Table 4.6. Values Used to Calculate Energy Level Impurity Appears to be Located within the Host KNbO₃ Crystal

\mathbf{Name}	Values
Madelung Energy Cr ³⁺ ionization energy	$E_M = -31.6 \text{ eV}$
Cr ^{**} ionization energy	$I_{Cr}=30.96 \text{ eV}$

The Madelung electrostatic potential found using the VESTA program in this research is the main contribution to the potential energy needed to hold the ionic crystal of KNbO₃ together. This electrostatic potential was used along with the ionization energy of Cr^{3+} in a vacuum as an attempt to verify the energy level position of the Cr^{3+} atom in a unit cell of KNbO₃. The coulombic potential or Madelung electrostatic potential was found to be, $E_M = -31.6$ eV.

Adding the Ionization energy of a free Cr^{3+} to the Madelung potential energy that was found using the VESTA program we find that

$$E_{calc2} = I_{Cr} + -E_M ,$$
 (4.11)

where E_{calc2} is 0.64 eV. Subtracting E_{calc2} from the known experimental bandgap of KNbO₃ will give information to where the energy level at which the Cr³⁺ impurity lies with respect to the CB.

$$E_{PI2} = 3.3eV - E_{calc2} (4.12)$$

 $E_{PI2} = 2.66$ eV found using the Madelung energy, through the VESTA program suggests that the Cr^{3+} photoionization energy would appear to be in the near infrared range, as initially suggested theoretically. This suggest that the impurity energy level lies 2.66 eV below the conduction band for a donor impurity.

Chapter 5

SPECTRAL ANALYSIS OF THE HOST KNBO3 AND KNBO3:X% CR3+

5.1 XRD PATTERN OF THE HOST KNBO $_3$ AND KNBO $_3$:x% CR $^{3+}$

The optical properties of KNbO₃ synthesized by the sol gel technique are discussed in this chapter. The samples of KNbO₃ fabricated by the sol gel synthesis technique form polycrystalline ceramics that have crystal dimensions on the order wavelengths of visible radiation. Due to the materials intrinsic scattering at these dimensions, the sol gel synthesized crystallites are opaque. In this case the use of X-ray diffraction (XRD) was necessary. XRD reveals the various phases of the sample and is important here since the orthorhombic phase of KNbO₃ is needed in order to match the theoretical models in this research project.

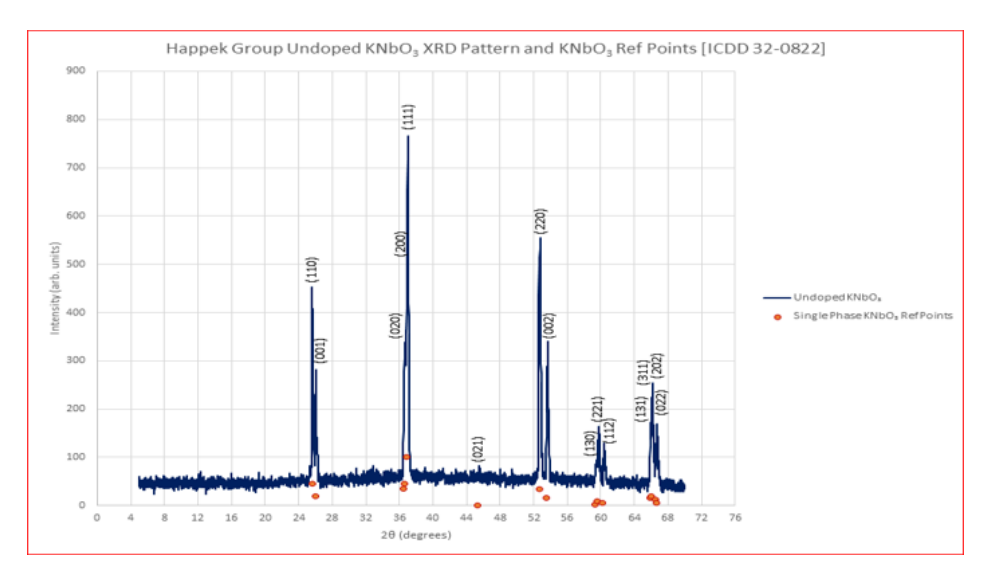


Figure 5.1: XRD of undoped KNbO₃ using Co K α fabricated in the Happek Lab.

As can be seen from XRD spectroscopy in Figure 5.1, the samples are verified to single phase orthorhombic KNbO₃. From the XRD pattern of the undoped KNbO₃ in Figure 5.1 it shows that the peaks are consistent with that of KNbO₃ from the International Centre for Diffraction Data [ICDD 32-0822]. This XRD pattern is consistent with that found by Tanaka et. al. as well; although the peaks in the pattern have shifted due to the use of a Co $K\alpha$, X-ray source instead of Cu $K\alpha$ source used by Tanaka et. al. A sintering temperature of 900°C was used to produce the calcined ceramics for this dissertation. This sintering temperature has been shown by K. Tanaka et. al. to produce single phase potassium niobate. By using a reflux temperature with the precursor materials it appears that the $K_4Nb_6O_17$ phase disappeared. Furthermore, the problem of significant loss of K_2O is avoided due to processing at the relatively low sintering temperature. Perovskite single phase KNbO₃was obtained from refluxing the precursor solution at 120°C using 2-methoxyethanol solvent and the perovskite peaks near $2\theta = 53.0^{\circ}$ split 220 and 002. An XRD pattern of the sol gel synthesized potassium niobate doped with varying amounts of Cr^{3+} are shown in Figure 5.2. From the XRD, there is no evidence of other phases in the sample.

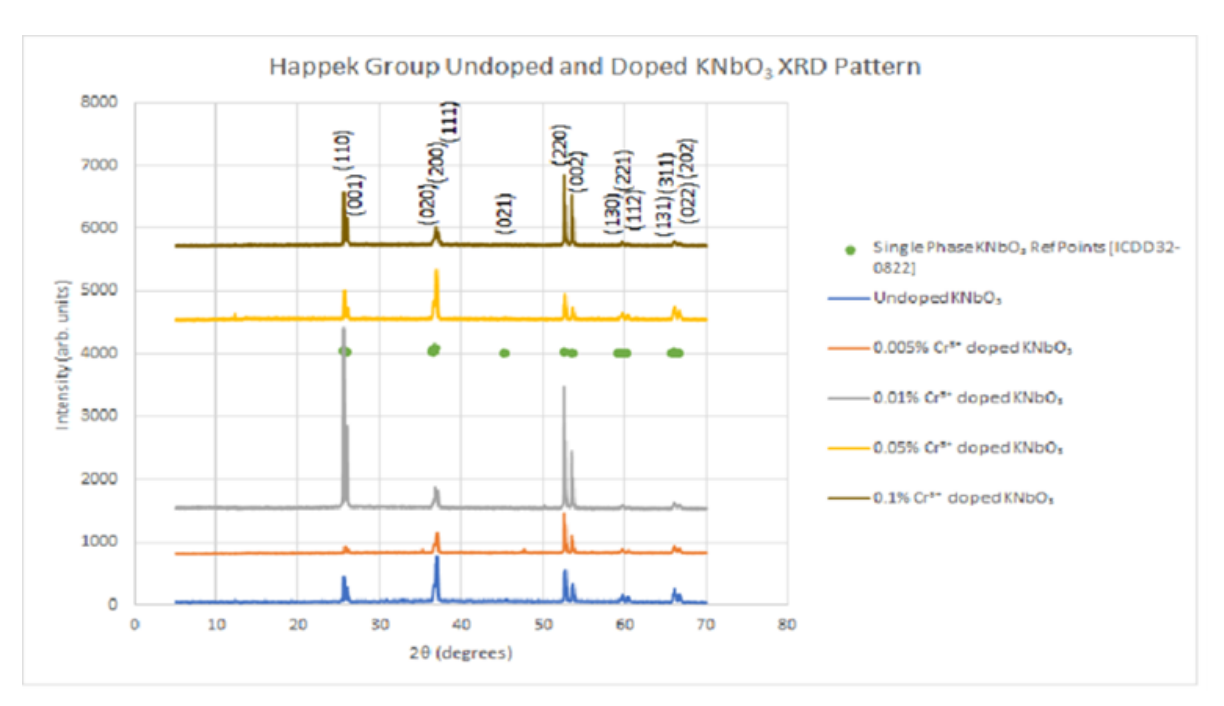


Figure 5.2: XRD of KNbO3: 0.005, 0.01, 0.05, and 0.1 mol% $\rm Cr^{3+}$ using Co K α fabricated in the Happek Group Lab.

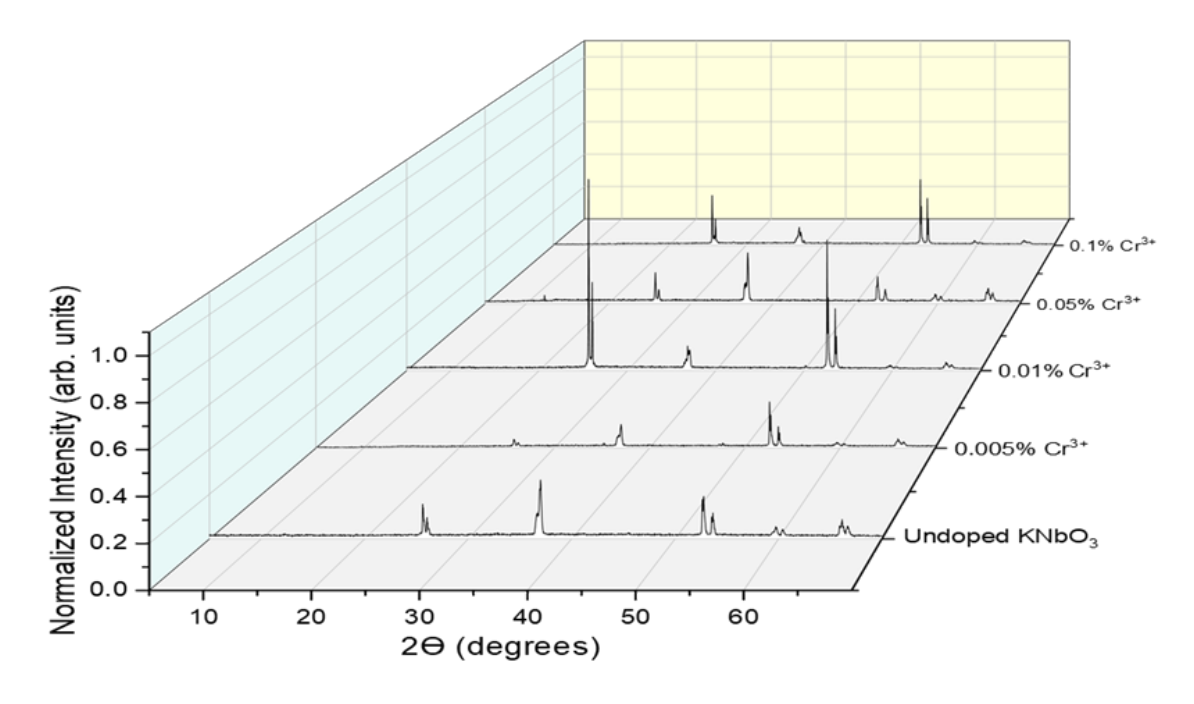


Figure 5.3: 3-D view of XRD of x% Cr^{3+} KNbO₃ using Co K α fabricated in the Happek Lab.

As can be seen in the Figures 5.2 and 5.3 there appears to be some differences in peak intensities as the percentage of Cr³⁺ is added. This may be due to ion size or the replacement of chromium ions in place of niobium atoms and reaching some saturation point The ionic radii of Nb⁵⁺ is 0.64 Åand Cr³⁺ is 0.62 Å. To futher this research and better understand what may be the cause of this change in intensities along with the change in mol % of trivalent chromium, Williamson Hall plots of the XRD are used in the next section of this research. The Williamson Hall plot can give us information on the stress and strain along with the crystallite size of the crystalline material that could contribute to the intensity changes.

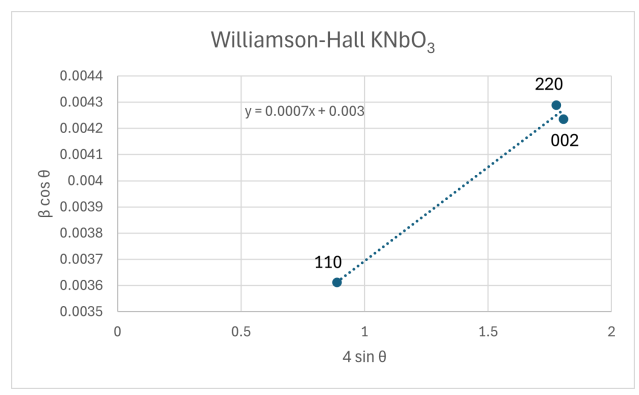
5.2 WILLIAMSON HALL ANALYSIS OF XRD PATTERN OF THE HOST KNBO $_3$ AND KNBO $_3$:X% CR $^{3+}$

From the XRD pattern of the undoped KNbO₃ in Figure 5.1 the peaks are consistent with that of KNbO₃ from [ICDD 32-0822.] No other secondary phases such as K₄Nb₆O₁7, K₂CO₃, or Nb₂O₅ were found which indicates the formation single phase KNbO₃. As can also be seen from Figure 5.2 the undoped sample is found to be orthorhombic in structure, due to the split of the diffraction peaks, (220) and (002) [56]. Past reports on KNbO₃ have shown that it goes through phase transitions from rhombohedral to orthorhombic at 10 °C, from orthorhombic to tetragonal at 225 °C and then from tetragonal to cubic at 435 °C temperature [57]. Therefore, in the current work an observed orthorhombic phase of KNbO₃ sample at room temperature agrees with these reports.

The Williamson-Hall graphs were plotted for each sample of KNbO₃ from the undoped as well as the KNbO₃:x% Cr^{3+} . The slopes of the Williamson Hall plots were approximated from the full widths at half maximum (FWHM) of the XRD reflection peaks of some of the most intense peaks, that showed changes with increased dopant percentages of Cr^{3+} which include (110), (220), and (002).

$$\beta cos\theta = D\epsilon sin\theta + \frac{\kappa\lambda}{L} \tag{5.1}$$

Where β is the FWHM, κ is the Scherrer constant, λ is the X-ray wavelength and ϵ is the microstrain. The slopes were determined by the following Williamson-Hall plots of peaks (110), (220), and (002) when the fits for the FWHM were possible for the peaks. All FWHM's were done using OriginLab 2018. Figures 5.4 - 5.8 show the Williamson-Hall plots for the host KNbO₃ and KNbO₃:x% Cr³⁺ where x is .005 - 0.1 mol%.



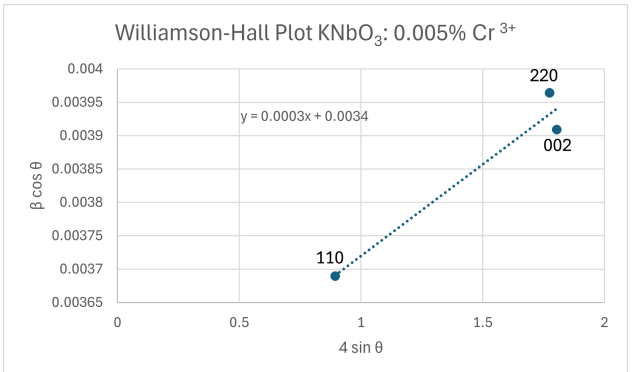
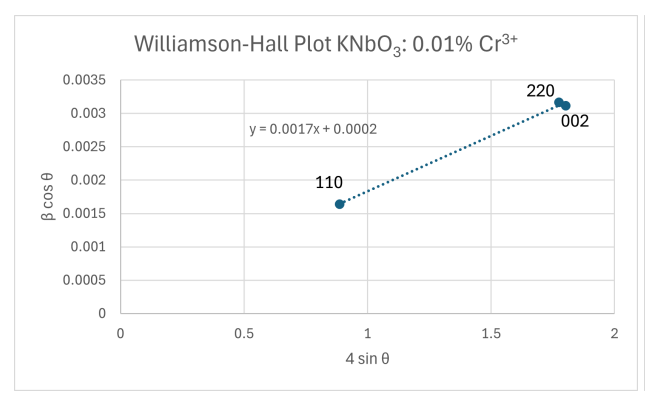


Figure 5.4: Williams-Hall Plot $\mathrm{KNbO_3}$

Figure 5.5: Williamson-Hall Plot KNbO3: 0.005 mol% $\rm Cr^{3+}$



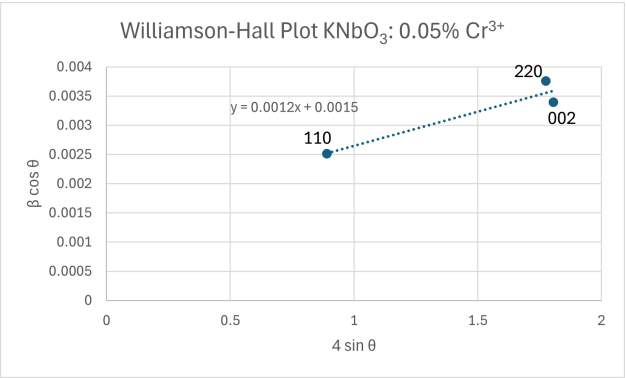


Figure 5.6: Williams-Hall Plot KNbO3: 0.01 Figure 5.7: Williamson-Hall Plot KNbO3: mol% $\rm Cr^{3+}$ 0.05 mol% $\rm Cr^{3+}$

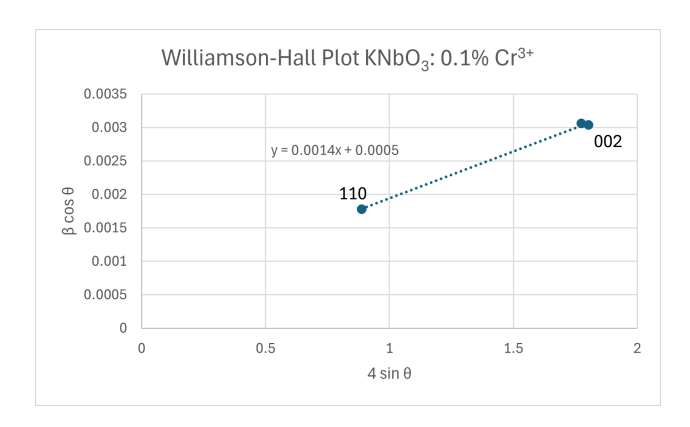


Figure 5.8: Williamson-Hall Plot KNbO₃: 0.1 mol% Cr³⁺

The positive value of the slopes indicates that the crystals are in tensile mode. Tensile mode refers to the behavior of crystalline materials when they are under tensile stress. Tensile stress is a force that attempts to stretch or elongate a material. This relates that the crystalline material is pulled and could be experiencing deformation. The response of the crystal to tensile stress depends on its atomic arrangement, bonding and other intrinsic properties. Which could be part of the cause in difference in XRD intensity peaks with the change in mol%.

Another aspect of the slpes from the Williamson-Hall plots of the host KNbO₃ and KNbO₃:x% Cr³⁺ where x is .005 - 0.1 mol% it can be seen that as the concentration of the dopant (Cr³⁺) increases, so does the slope of the line-fit up to what appears to be a saturation point, then the slope begins to decrease. This could be due to microstrain or change in crystallite structure. The slope of these lines provide the value of the intrinsic strain. The origin of the lattice strain mainly comes from the lattice expansion or contraction in the nanocrystals due to size confinement. However, many defects also get created at the lattice structure due to size confinement which can result in lattice strain.

From the information found in the Williamson-Hall plots in Figures 5.4 - 5.8 the crystallite size can be found. Using the y-intercept from the line fit given in each figure the

crystallite size can be estimated. The y-intercept from each slope is equated to the Scherrer equation for Figures 5.4 - 5.8 that correspond to the increasing mol% of dopant that was added to the KNbO₃ host lattice respectively.

$$y - intercept = \frac{0.9\lambda}{L} \tag{5.2}$$

Where 0.9 is the shape factor, λ is the wavelength of the X-ray source (in this case is λ = 1.79 Å).

Table 5.1. Values of crystallite sizes of KNbO $_3$ and KNbO $_3$:x% Cr $^{3+}$ where the concentration of Cr $^{3+}$ is increased from 0.005 to 0.1 mol%

Polycrystalline Material	Values for Crystallite Size
KNbO ₃	53.7 nm
$KNbO_3$: 0.005 mol% Cr^{3+} $KNbO_3$: 0.01 mol% Cr^{3+}	$47.4 \mathrm{nm}$ $805.5 \mathrm{nm}$
KNbO ₃ : 0.05 mol% Cr ³⁺ KNbO ₃ : 0.1 mol% Cr ³⁺	$107.4 \mathrm{nm}$ $322.2 \mathrm{nm}$

The changes in crystallite size can provide some insight into the structural and compositional changes of a host material such as $\mathrm{KNbO_3}$ when doped with an increasing $\mathrm{mol\%}$ of Cr³⁺. One effect of doping that could possibly cause a change in crystallite size is peak broadening. The width of diffraction peaks is inversely related to the crystallite size according to the Scherrer equation. This could show that as the molar percentage of the dopant is increased and the crystallite size decreases, the peaks in the XRD pattern may become broader. Conversely in the case of this research there appears to be some peak narrowing as the dopant is increased to 0.01 mol\% showing that there is some possible peak narrowing. However as the mol% of the Cr³⁺ continues the crystallite size appears to decrease which suggests peak broadening. Intensity of XRD peaks can also be changed by the amount of polycrystalline material present but also by the crystalline structural changes. Doping can introduce defects or alter symmetry of the crystal lattice, where in the case of this research the structural changes could be due to the size difference of Nb⁵⁺ and Cr³⁺ along with the possible charge compensation causing a loss of an oxygen anion. Since the dopant occupies lattice sites within the host structure this can cause changes within the periodic arrangement of atoms, which can potentially decrease the intensity of certain peaks while increasing the intensity peaks in others. From Table 5.1 it can easily be seen that as the mol\% is increased so to is the crystallite size up to some saturation point where the most intense peaks at $\mathrm{KNbO_3}$ doped with 0.01 mol% of $\mathrm{Cr^{3+}}$ and the largest estimation of the crystallite size of 805.5 nm.

CHAPTER 6

Conclusions

In summary the figures and narrative show that KNbO₃ doped with Cr³⁺ ions is photorefractive in the NIR. Single phase KNbO₃ and KNbO₃:x% Cr³⁺ were derived using the sol-gel method. The experiments confirm that sol-gel fabricated potassium niobate is highly stoichiometric and does not contain any other phases of potassium niobate.

For the crucial parameter of the location of the impurity groundstate with respect to the conduction band, theoretical calculations were made using the nearest neighbor Madelung potential and the Madelung energy that was calculated using the VESTA program both with Oxygen and Niobium vacancies for the parameter of charge compensation [8]. The results from the nearest neighbor Madelung potential in conjuction with the ionization energy of Cr³⁺ in a vacuum and the Madelung lattice energy calculated using the VESTA program to find the photoionization energy of Cr³⁺ within the host KNbO₃ were in agreement with the sugggestions from theoretical computational research of Bhattacharya et. al. [3] and Sutter et al [12].

XRD experimental data was analyzed theoretically by Williamson Hall plots. The Williamson Hall plots showed an appearance of some correlation with microstrain and change in intensity of XRD peaks when the Cr³⁺ dopant was added in rising percentages. This could be interpreted as a dependence on the atomic structure of the dopant causing lattice defects and dislocations. Aother aspect of Williamson-Hall plot is using the y-intercept to estimate crystallite size. Crystallite size can influence optical properties of a material which is crucial

in this research. The crystallite size went up to a maximum size of 850 nm as the dopant concentration went up to 0.01 mol%. This could show that at a minimum or maximum crystallite size could relate to optimal optical properties. This may in turn show that the proper crystallite size will have a photoionization energy in the NIR. With further experimental research a correlation to the crytallite size and optium optical properties could possibly be shown using Fourier Transform Infrared (FTIR) and Photoconductivity measurements of each doped sample of KNbO₃.

Chapter 7

FUTURE WORK

It has been shown that KNbO₃:x% Cr³⁺ appears to be photorefractive in the near infrared. For an experimental understanding of the location of the impurity groundstate with respect to the host valence and conduction bands, photoconductivity or similar optical techniques are useful. If samples are available in polycrystalline form only, IR stimulated luminescence is the preferable technique to find the location of impurity energy levels within the host bandgap, provided the impurity center does not luminesce. Briefly, in this technique the sample is irradiated at a fixed frequency at low temperature for a pre-defined period. The illumination is then turned off, and the sample is either heated up and thermoluminescence is observed or the sample is irradiated with infrared radiation and IR-stimulated radiation of the impurity is observed. The important point in both versions is that the stimulated luminescence requires trapped charges that have or have not been filled during the initial, optical, illumination process. If the energy of the optical excitation is sufficient to promote an electron to the conduction band thermoluminescence and IR-stimulated radiation is observed.

On the other hand, if the photon energy is insufficient to bridge the gap between impurity ground state and host band, no traps can be filled, and no stimulated luminescence can be observed. Therefore, by systematically varying the excitation photon energy from low to higher energy and searching for stimulated luminescence after each illumination process, a threshold can be established at which the photon energy is just sufficient to promote electrons into the host conduction band. This energy then is the desired energy difference

between the impurity ground state and the host conduction band. If the impurity ion does not luminesce (which is likely the case if the groundstate lies at an energy of less than 1 eV below the conduction band), photoconductivity experiment will be performed: A pair of electrons are pressed onto the sample at a distance of about 1 mm and a potential difference of about 1,000 V is applied. The gap between the electrodes is then illuminated with the output of a tuneable light source. While the light source is scanned from low to high photon energies, the current between the electrodes is recorded. When the photon energy is sufficient to promote impurity electrons into the conduction band; the current, which is proportional to the carriers in the conduction band will increase and the location of the impurity ground state relative to the conduction band can be established. Concerning the photoconductivity measurements; it is problematic to lower the temperature of the polycrystalline chromium doped potassium niobate due to phase changes that occur when the experimental material is lowered far below room temperature. When this material changes phases it also changes electroptic properties of orthorhombic potassium niobate in general.

BIBLIOGRAPHY

- [1] Matthias BT and Remeika JP. Ferroelectricity in the ilmenite structures. *Phys. Rev.*, 76(1886-1887), 1949.
- [2] A. W. Hewat et al. Cubic-tetragonal-orthorhombic-rhombohedral ferroelectric transitions in perovskite potassium niobate: Neutron powder profile refinement of the structures. J. Phys. C: Solid State Phys, 6(16):2559 -2572, 1973.
- [3] M. Bhattacharya. First-Principles Studies of the Effects of Transition Metal Impurities on the Electronic Structure of KNbO₃. PhD thesis, University of Georgia, 2014.
- [4] K. Tanaka, K. Kakimoto, and H. Ohsato. Morphology and crystallinity of knbo₃-based nano powder fabricated by sol-gel process. *Journal of the European Ceramic Society*, (27):3591–3595, 2007.
- [5] Y. Yoshikawa, T. Asaka, M. Higuchi, Y. Azuma, and K. Katayama. Effects of exess k₂0 and processing conditions on the preparation of dense k(ta_{1-x}nb_x)o₃ ceramics. Ceramics International, 34:609-613, 2008.
- [6] B. Henderson and G. F. Imbusch. Optical Spectroscopy of Inorganic Solids. Oxford University Press, 2006.
- [7] U. Happek, S.A. Basun, J. Choi, J.K. Krebs, and M. Raukas. Electron transfer processes in rare earth doped insulators. *Journal of Alloys and Compounds*, 303-304:198–206, 2000.
- [8] K. Momma and F. Izumi. Vesta 3 for three-dimensional visualization of crystal volumetric and morphology data. *Journal of Applied Crystallography*, 44:1272–1276, 2011.

- [9] Peter Gunter and Jean-Pierre Huignard. Photorefractive Materials and Their Applications 1. Springer Science and Business Media, Inc., 2006.
- [10] M. Zgonik M. Ewart C. Medrano and P. Gunter. Phototrefractive effects in knbo₃.
 Springer Series in Optical Sciences, (205-240), 2007.
- [11] E.G. Suter. AB Initio Studies of Dopant-Defect Complexes in KNbO₃. PhD thesis, University of Georgia, 2022.
- [12] E.G. Suter, M. Bhattacharya, S. Lewis, and W. Dennis. Effects of transistion metal dopants on the electronic structure of potassium niobate. *Journal of Applied Physics*, 131, 2022.
- [13] F.M. Michel-Calendini, M. Peitier, and F. Micheron. Electron paramagnetic resonance of fe³⁺ in orthorhombic knbo₃. Solid State Communications, 33:145–150, 1980.
- [14] S. Brulisauer, D. Fluck, P. Gunter, L. Beckers, and C. Buchal. Controlled reduction of fe-doped knbo₃ by proton-irradiation. Optics Communication, 153:375–386, 1998.
- [15] P.D. Durugkar. Dielectric dispersion in pure, samarium, samarium and tin doped potassium niobate single crystals. *Ferroelectrics*, 540(1):54–64, 2017.
- [16] V.V.Galutskii, E.V. Stroganova, and N.A. Yakovenko. Spectral separation of cr³⁺ optical centers in stoichiometric magnesium-doped lithium niobate crystals. *Condensed-Matter Spectroscopy*, 110(3):401–407, 2010.
- [17] H. Al-Ghamdi, N.A.M Alsaif, Z.Y.Khattari, M.S. Shams, A.M. El-Refaey, M.S. Sadeq, Y.S. Rammah, R.A. Elsad, M.A. El-Shorbagy, and S.M. Shaaban. Exploring the physical, vibrational, optial, and dielectric properties of chromium-doped bismoborate barium glasses for potential use in optical applications. *Optical and Quantum Electronics*, 55(904), 2023.

- [18] I. Halemah and El-Saeedy. Impact of controlled doses on enhancement of structural, optical, and electrical properties in chromium-doped cadmium oxide cap layers for enhancing n-cco/p-si solar cells performance. Optical Materials, 162(116859), 2025.
- [19] K.C. Mishra P.C. Schmidt and K. H. Johnson. Bands versus bonds in electronic-structure theory of metal oxides: Application to luminescence of copper in zinc oxide. *Physics Review B*, 42(2), 1990.
- [20] W. Ching M-Z. Huang and Y-N Xu. First-principles calculation of optical properties of c₆₀ in the fcc lattice. *Physical Review Letters*, 67(15), 1991.
- [21] W. Ching and M-Z. Huang. Electronic and optical properties of yttria. *Physical Review Letters*, 65(7), 1990.
- [22] K. Mishra J. Berkowitz B. DeBoer and E. Dale. Electronic structure and associated properties of europium-activated strontium tetraborate phosphor. *Physical Review* B, 37(13), 1988.
- [23] J. Guertin, J. Alan, and C. P. Avakian. Chromium (VI) Handbook. CRC Press, 2005.
- [24] W.N. Cottingham. An Introduction to Nuclear Physics. New York Cambridge University Press, 1987.
- [25] P. Grevatt. Toxicological review of trivalent chromium. U.S. Environmental Protection Agency, 1998.
- [26] E. Rai, R.S. Yadav, D. Kumar, A.K. Singh, V.J. Fulari, and S.B. Rai. Structural and photoluminescence properties of cr³ doped lavo₄ phosphor. Solid State Sciences, 129, 2022.
- [27] R.S. Yadav and S.B. Rai. Concentration and wavelength dependent frequency down-shifting photoluminescence from a tb³⁺ doped yttria nano-phospho: A photochromic phosphor. *Journal of Physics and Chemistry of Solids*, 114(179-186), 2018.

- [28] J.N. Lalena, D.A. Cleary, and O.B.M. Hardouin Duparc. Principles of Inorganic Materials Design Third Edition. Wiley, 2010.
- [29] R. H. Bube. Photoconductivity of Solids. John Wiley & Sons, Inc., 1960.
- [30] D. Morris and E. Short. The born fajans haber correlation. Nature, 224(950-952), 1969.
- [31] W. Wong and D. McClure. Charge-exchange processes in titanium-doped sapphire crystals. i. charge-exchange energies and titanium-bound excitons. *Physical Review B*, 51(9), 1985.
- [32] A. Ashkin, G.D. Boyd, J.M. Dziedzic, R.G. Smith A.A. Ballman, J.J. Levinstein, and K. Nassau. Optically-induced refractive index inhomogeneities in linbo₃ and litao₃. Applied Physics Letters, 9(1), 1966.
- [33] F.S. Chen. A laser-induced inhomogeneity of refractive indices in ktn. *Journal of Applied Physics*, 38:3418–3420, 1967.
- [34] J.J. Amodei. Electron diffusion effects during hologram recording crystals. *Applied Physics Letters*, 18:22–24, 1971.
- [35] J.J. Amodei, W. Phillips, and D.L. Staebler. Improved electrooptic materials and fixing techniques for holographic recording. *Optica Publishing Group*, 11(2):390–396, 1972.
- [36] A.M. Glass, D. Von Der Linde, and T.J. Negran. Improved electrooptic materials and fixing techniques for holographic recording. Optica Publishing Group, 11(2):390–396, 1972.
- [37] Mitsubishi Chemical. https://technical.gelest.com/brochures/reactive-silicones/polymeric-metal-alkoxides.
- [38] T. J. Hall R. Jaura L. M. Connors and P. D. Foote. The photorefractive effect-a review.

 Progress in Quantum Electronics, 10(77-146), 1985.

- [39] Robert Boyd. Nonlinear Optics. Harcuort Brace Jovanovich, Publishers, 1992.
- [40] G. Williamson and W. Hall. X-ray line broadening from filed aluminium and wolfram.

 Acta Metallurgica, 1:22–31, 1953.
- [41] Md. Hossain and S. Ahmed. Easy and green synthesis of tio₂ (anatase and rutile): Estimation of crystallite size using scherrer equation, williamson-hall plot, monshi-scherrer model, size-strain plot, halder-wagner model. Results in Materials, 20(100492), 2023.
- [42] K. Shih. X-ray Diffraction: Structure, Principles, and Applications. Nova Science Publishers, Inc, 2013.
- [43] B. Cullity an S. Stock. *Elements of X-ray Diffraction*. Pearson Education Limited, 2014.
- [44] D.J. Newman and Betty Ng. Crystal Field Handbook. Cambridge University Press, 2000.
- [45] Y. Tanabe and S. Sugano. On the absorption spectra of complex ions. J. Phys. Soc. Jpn, 9(753-756), 1954.
- [46] Charles Kittel. Introduction to Solid State Physics, 7th Ed. John Wiley & Sons, 1996.
- [47] Harald Ibach and Hans Luth. Solid-State Physics An Introduction to Principles of Materials Science. Springer-Verlag Berlin Heidelberg, 2009.
- [48] V. Goldschmidt. Die gesetze der krystallochemie. *Die Naturwissenschaten*, pages 14:477–485, 1926.
- [49] W. Van Gool and A. Piken. Lattice self-potentials and madelung constants for some compounds. *Journal of Materials Science*, 4:95–104, 1969.

- [50] Y. Waseda, E. Matsubara, and K. Shinoda. X-Ray Diffraction Crystallography. Springer New York, NY, 2011.
- [51] G. Harrington and J. Santiso. Back-to-basics tutorial: X-ray diffraction of thin films.

 Journal of Electroceramics, 47:1–23, 2021.
- [52] C. J. Brinker and G.W. Scherer. Sol-gel science: The physics and chemistry of solgel processing. Academic Press, Inc., 1990.
- [53] D. R. Lide and H. P. R. Frederikse. CRC Handbook of Chemistry and Physics, 75th Ed. Chemical Rubber Publishing Company, 1994.
- [54] A.Z. Simoes, A. Ries, C.S. Riccardi, M.A. Zaghete, and J.A. Varela. Optical properties of potassium niobate thin films prepared by the polymeric precursor method. *Materials Letters*, 2004.
- [55] Gh. H. Khorrami, A. Kompany, and A. Khorsand Zak. Structural and optical properties of (k, na)nbo₃ nanoparticles synthesized by a modified sol-gel method using starch media. *Advanced Powder Technology*, 26(113-118), 2015.
- [56] M.R. Joung, H. Xu, J.S. Kim, I.T. Seo, S. Nahm, J.Y. Kang, and S.J. Yoon. Structural variation of hydrothermally synthesized knbo₃ nanowires. *Journal of Applied Physics*, 111(114314):1–5, 2012.
- [57] R. Balakrishnaiah, D.W. Kim, S.S. Yi, K.D. Kim, S.H. Kim, K. Jang, H.S. Lee, and J.H. Jeong. Fluorescence properties of nd³⁺-doped knbo₃ phosphors. *Electrochemical and Solid State Leeters*, 12(7):J64–J68, 2009.